

Original papers

Classification of maize lodging types using UAV-SAR remote sensing data and machine learning methods



Dashuai Wang^a, Minghu Zhao^a, Zhuolin Li^a, Xiaohu Wu^a, Nan Li^b, Decheng Li^b, Sheng Xu^c, Xiaoguang Liu^{a,*}

^a School of Microelectronics, Southern University of Science and Technology, Shenzhen 518055, China

^b Shenzhen Institute of Artificial Intelligence and Robotics for Society, Shenzhen 518129, China

^c Shenzhen Institute of Advanced Technology, Chinese Academy of Sciences, Shenzhen 518055, China

ARTICLE INFO

Keywords:

Maize lodging
Unmanned aerial vehicles
Synthetic aperture radar
Machine learning
Radar backscattering coefficient

ABSTRACT

Lodging seriously threatens maize quality and yield and inevitably increases management and harvest costs. Timely collection of crop lodging information plays a pivotal role in the post-disaster assessment and agricultural insurance claims. Although spaceborne radar and optical remote sensing have unparalleled advantages in obtaining large-scale agricultural information, their response capacity to sudden natural maize lodging disasters is insufficient due to the limited spatial-temporal resolution of the satellite data. In recent years, the widespread application of unmanned aerial vehicles (UAVs) based optical remote sensing in precision agriculture has provided an effective alternative to spaceborne remote sensing. However, optical sensing can only effectively reveal the reflectance spectral characteristics of lodging maize under good lighting conditions. This work proposes a novel maize lodging classification method based on UAV synthetic aperture radar (UAV-SAR) and machine learning to circumvent the limitations of spaceborne and UAV-based remote sensing in monitoring maize lodging. Firstly, the raw radar remote sensing data of our study area containing lodging and non-lodging maize plants at the maturity stage is collected by the custom-built X-band and Ku-band UAV-SAR systems. Secondly, the corresponding backscattering coefficients and radar vegetation indices in each lodging type are extracted through radiation calibration and band math. Subsequently, the impacts of radar parameters (bands, polarizations, and observation orientations) and lodging types on backscattering coefficients are comprehensively analyzed. Fourthly, we applied the recursive feature elimination (RFE) algorithm to identify significant feature subsets and constructed multiple datasets using ten filter scales. Finally, five machine learning models (XGBoost, LDA, RF, KNN, and ANN) are trained and tested based on these materials. The classification results under different filter scales and feature combinations show that ANN achieves the best performance with an overall accuracy of 98.26 % and a Kappa coefficient of 0.982. This is the first innovative study successfully introducing cutting-edge UAV-SAR into maize lodging monitoring. Following spaceborne optical, spaceborne radar, and UAV-based optical remote sensing technologies, UAV-SAR holds great potential as the fourth practical means for collecting high-resolution agricultural information.

1. Introduction

Crop lodging, including stem lodging and root lodging, is defined as the state of permanent displacement of the stem or root from an upright position (Pithus, 1974). Lodging usually damages the morphological structure of crops, thereby disrupting the vital processes of nutrient transport and photosynthesis. As a result, it seriously affects the yield and quality of crops and increases management and harvest costs,

ultimately reducing farmers' production profits. Maize, a tall stem crop commonly cultivated throughout the world, is highly susceptible to lodging stress, which is usually triggered by the interaction of genetically determined lodging resistance, extreme weather (e.g., long-term heavy rainfall, strong winds, unforeseen hail), and improper management (e.g., dense planting, excessive nitrogen application, pests, and diseases). Timely and accurately acquiring maize lodging parameters, such as occurrence, incidence, type, area, severity, and distribution, are

* Corresponding author.

E-mail address: liuxg@sustech.edu.cn (X. Liu).

crucial for post-disaster rescue management and agricultural insurance claims. However, this remains a significant challenge given the unpredictability of lodging hazards, the temporal-spatial heterogeneity of lodging distribution, the accessibility of multi-scale and multi-mode data, etc.

Maize plants affected by lodging usually suffer changes in physiological characteristics (e.g., pigment content and photosynthesis) and morphological traits (e.g., canopy structure and plant height). Conventional observation methods mainly include manual *in-situ* surveys, spaceborne remote sensing, and UAV-borne optical remote sensing. *In-situ* surveys are labor-intensive, time-consuming, empirical-dependent, subjective-prone, and impractical for large-scale observation immediately after lodging occurs. Nevertheless, manual observation remains crucial in lodging assessment because the actual data from on-site observations serves as ground truth for evaluating the effectiveness of some model-based inversion models (Guan et al., 2022a). Technological advancements in agricultural remote sensing have enabled farmers to improve productivity effortlessly. Specifically, spaceborne optical remote sensing, spaceborne synthetic aperture radar (SAR) remote sensing, and UAV optical remote sensing have become powerful tools for farmland monitoring and lodging assessment (Chauhan et al., 2019).

With the improvement of their spatial and temporal resolution, spaceborne optical sensors have been successfully used to capture the spectral reflectance difference of lodging crops at a large scale. The raw bands and derived vegetation index (VI) are the primary inputs of the inversion model for maize lodging parameters. Guan et al. (2022b) investigated the spectral response (including selected spectral bands and VIs) of Sentinel-2 under different lodging percentage levels and constructed a random forest-based quantitative model to estimate lodging percentage. Similarly, to monitor the lodging extents of maize crops, Qu et al. (2022) derived a variety of features (spectrum, texture, VIs) from multitemporal Gaofen-1(GF-1) images and analyzed the sensitivity of different features. Based on these results, the authors obtained the optimal feature combination through the recursive feature elimination method and achieved 87.5 % lodging extent classification accuracy via the random forest classifier. However, it is worth noting that optical remote sensing is a passive remote sensing method, which means that it relies on passively receiving the reflection signal of sunlight from ground objects. As such, the availability, quality, and timeliness of satellite optical remote sensing images are heavily dependent on meteorological conditions.

Synthetic aperture radar (SAR) is an active imaging radar mounted on a moving platform. SAR actively transmits electromagnetic waves of specific or modulated frequencies and then collects the backscattered echoes by the radar antenna. The electromagnetic waves have outstanding cloud and fog penetration capabilities, making SAR remote sensing largely independent of meteorological conditions and able to collect radar images during the day and night (Moreira et al., 2013). Since SAR signals are sensitive to morphological variations of ground objects, satellite-based SAR remote sensing has been successfully used in agricultural lodging monitoring (Hashemi et al., 2024). Sentinel-1, RADASAT-2, and Gaofen-3 (GF-3) are the most common radar data sources among orbiting satellite radar sensors. A pioneering work in 2015 (Yang et al., 2015) demonstrated the effectiveness of fully polarized SAR for crop lodging monitoring. The authors extracted backscattering intensity and polarization features from C-band RADASAT-2 remote sensing images and studied the sensitivity of these features to characterize wheat lodging. Inspired by this work, there have also been studies on lodging monitoring of crops such as maize and rice based on different SAR data sources and features. Specifically, Guan et al. (2022a) proposed a new framework to estimate maize lodging area at the regional scale using multiple features such as backscatter coefficient, polarization decomposition, and radar vegetation index extracted from Sentinel-1 and GF-3. An important contribution of this study is that they analyzed the scattering mechanism of radar signals in lodging maize and found that as the severity of lodging increases, the depolarization effect

and scattering randomness of radar signals gradually weaken, and surface scattering quickly increases and then dominates the total scattering after lodging percentage exceeds 80 %. In addition to the above-mentioned SAR features, some studies have revealed that interference coherence is also an effective indicator for inverting crop lodging parameters using SAR images (Romero-Puig and Lopez-Sanchez, 2021).

As the diversity of radar data increases, multi-source, multi-mode, and multi-temporal feature fusion becomes an effective solution to reduce the uncertainty of lodging assessment models (Zhou et al., 2020a; Qu et al., 2023). For instance, Chauhan et al. (2020) assessed the potential of Sentinel-1(SAR) and Sentinel-2(Multispectral) time-series data for detecting wheat lodging incidence and severity under different growth stages and analyzed the effect of lodging on the backscatter, coherence, and spectral response. This study highlighted that the combination of physical and physiological characteristic information of lodging crops has great potential to improve the performance of the lodging parameter inversion models. Although spaceborne remote sensing plays a pivotal role in routine large-scale macroscopic observation, it also suffers several inherent limitations such as fixed revisiting cycles, low flexibility, and low spatial resolution. In certain scenarios, this may result in insufficient first-time response capabilities to unpredictable natural disasters, including maize lodging.

The past decade has witnessed a significant advancement in unmanned aerial vehicle technology and high-performance miniature sensors. In precision agriculture, high spatial-temporal resolution UAV remote sensing has become a versatile solution to break through the limitations of satellite remote sensing (Maes and Steppe, 2019). One of the successful cases is the application of UAV optical (e.g., RGB, Multispectral, Hyperspectral, LiDAR) remote sensing in crop lodging monitoring. The overall research pipeline can be roughly divided into four parts: data acquisition, feature extraction and selection, model construction, and performance evaluation. In the data acquisition stage, UAV-based digital imagery has become the most popular and mature method due to its high flexibility, easy availability, and low cost. In addition, there are also some works that use expensive multispectral, hyperspectral, and LiDAR sensors to monitor crop lodging. In terms of feature extraction and selection, numerous features such as color, texture, vegetation index, and canopy structure are usually extracted first, and then their correlation and sensitivity to crop lodging are analyzed, finally, the optimal feature combination is selected by feature screening algorithms. Linear or nonlinear regression and machine learning are commonly used models for retrieving crop lodging parameters. In addition, with the penetration of computer vision technologies in precision agriculture, deep learning has also been applied to classify crop lodging severity and segment the lodging area.

As synthetic aperture radars become increasingly miniaturized and integrated, their integration with UAVs becomes possible (Hügler et al., 2018; Abushakra et al., 2021). Compared to satellite-based SAR, UAV-SAR opens up new possibilities in the remote sensing community by offering the unique observational flexibility that is crucial for time-critical and fast dynamic applications. A simple and general idea is to transfer existing satellite SAR remote sensing technologies to UAV-SAR. For example, since 2009, Acevo-Herrera and colleagues have been paying continuous attention to the development of UAV deployable multi-frequency and full-polarized SAR systems, such as FMCW C-Band (5.3 GHz) SAR, L-Band(1.4 GHz) radiometer, and the first fully polarimetric SLFM-CW X-band(9.65 GHz) SAR (Acevo-Herrera et al., 2009). In 2012, Remy et al. (2012) built the first compact and flexible UAV-based P-(repeat-pass) and X-band (single-pass) interferometric SAR(InSAR) system and tried to apply UAV-InSAR to topographic survey and deformation measurement. Furthermore, as an extension of UAV-InSAR, UAV-based tomography SAR (UAV-TomoSAR) is a promising means to achieve 3D mapping (Wang et al., 2023).

Although UAV-SAR technology has made great progress, it still faces some technical challenges. A significant difference between UAV-SAR and satellite-SAR is that the instability of speed and attitude caused by

airflow disturbance will lead to errors between actual and nominal flight trajectories. These undesirable deviations can cause SAR image defocus and geometric distortion. Motion error compensation and focusing algorithms are two core technical problems that need to be addressed for high-resolution UAV-SAR imaging (Xing et al., 2009; Bekar et al., 2021). In addition, UAV radar remote sensing has stricter requirements on the compactness, lightweight, power consumption, processing ability, and position accuracy of the SAR system, which makes its practical applications relatively rare.

High-quality remote sensing images with high spatial-spectral-temporal-radiometric resolution are crucial for multi-scale crop lodging assessment. Although spaceborne optical, spaceborne SAR and UAV-based optical remote sensing play a crucial role in crop lodging monitoring, to the best of our knowledge, UAV-SAR, as a new technology branch for crop lodging assessment, has not yet been explored. To fill this gap, this work aims to make the first attempt to classify maize lodging types by deploying cutting-edge UAV-SAR and machine learning. Fig. 1 depicts the pipeline of this work, which can be briefly

divided into five stages: experimental design, data collection, data analysis, dataset construction, and machine learning-based classification models. The highlights and contributions of this study are summarized as follows:

- (i) As far as we know, this is the first exploration to apply the cutting-edge technology of UAV-SAR to maize lodging classification.
- (ii) We comparatively analyzed the radar responses of maize plants in different lodging states under different UAV-SAR bands, polarizations, and observation orientations.
- (iii) We constructed datasets containing backscattering coefficients and radar vegetation indices and extracted significant feature combinations through correlation analysis and feature selection algorithm.
- (iv) We evaluated the performance of five widely used machine learning-based algorithms for classifying maize lodging types with different SAR coherent noise suppression filter scales and feature combinations.

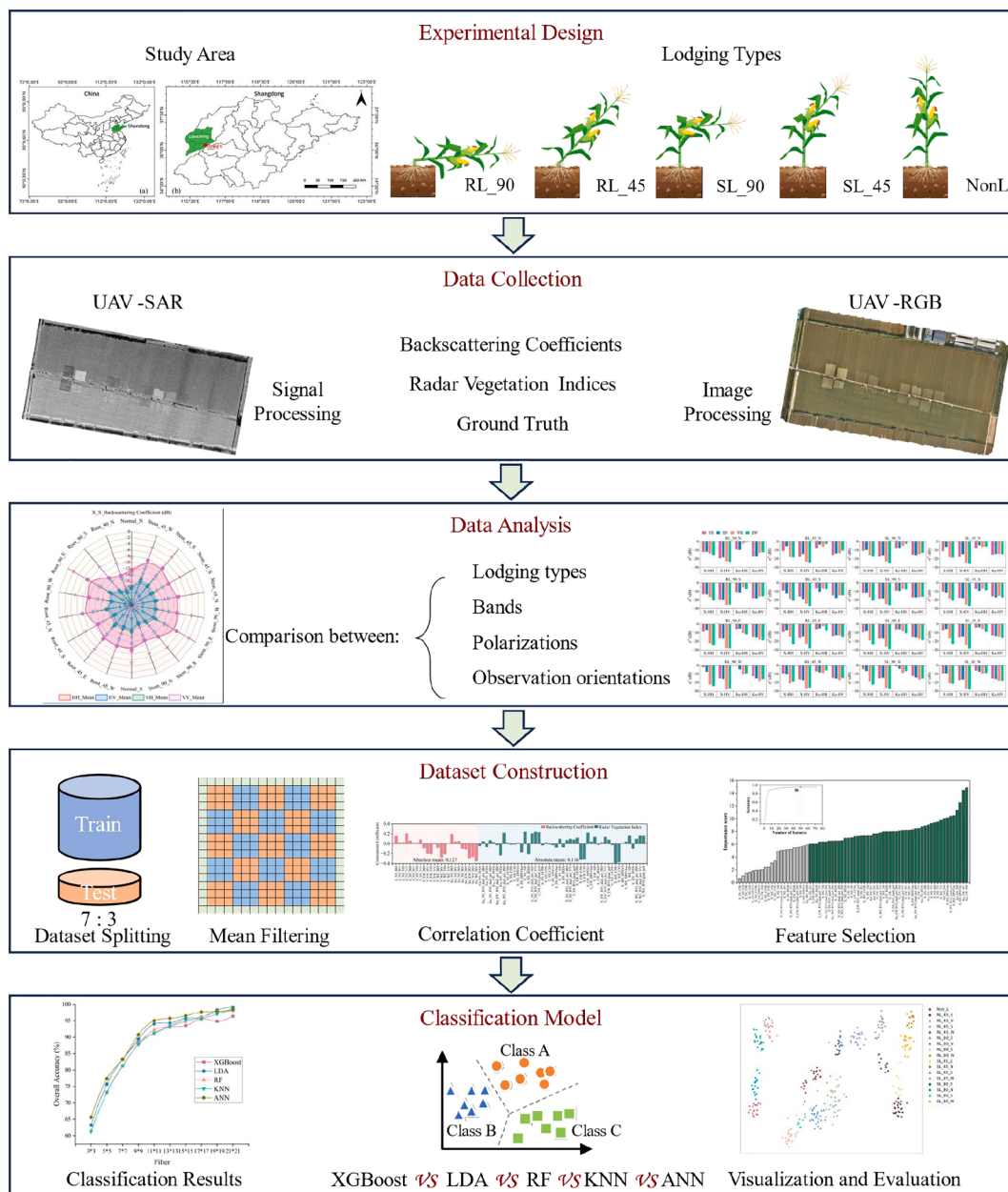


Fig. 1. The pipeline of this work.

2. Materials and methods

2.1. Study area

The study area is located in Dong'e County, Liaocheng City, Shandong Province, China (Fig. 2a and b). Dong'e County is a traditional maize-planting region with a temperate monsoon continental climate and four distinct seasons. The local average annual temperature is 14.48°C, the annual average relative humidity is 66 %, and the annual average precipitation is 556.9 mm. The maize experimental field

(Fig. 2c) covers an area of approximately 262,500 m² (750 m × 350 m). A road across the experimental field serves as the dividing line between the north and south experimental areas. The maize breed in the northern experimental area is MY73, and that in the southern experimental area is Lenong87. The direction of the planting ridge is parallel to the left border of the study area. The sowing date is June 10, 2023, the planting density is 67,500 plants/hectare, and the harvest date is October 2, 2023.

There are significant differences in the canopy structure of maize under different lodging states, and these changes will directly affect the

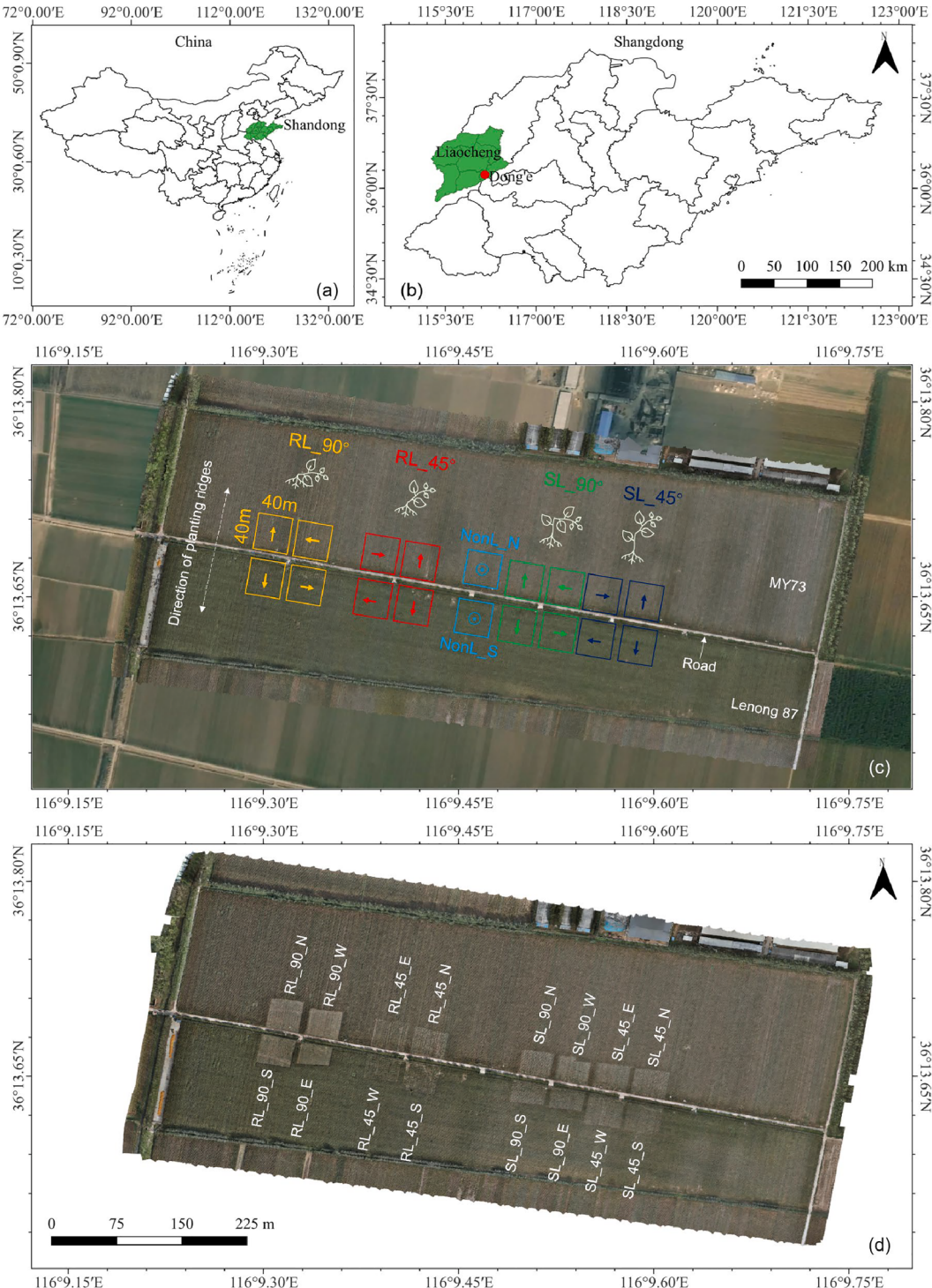


Fig. 2. Overview of the study area.

scattering characteristics of microwave signals, which constitute the physical basis for high-resolution UAV-SAR monitoring of maize lodging at the local farmland scale. In order to study the influence of maize lodging type on backscattering characteristics under different radar parameters as accurately as possible, we artificially created maize lodging experimental conditions. As shown in Fig. 2c, we defined four lodging types, namely 90° root lodging (RL_90), 45° root lodging (RL_45), 90° stem lodging (SL_90), and 45° stem lodging (SL_45). In addition, each lodging type includes four subcategories with lodging orientation towards north, south, east, and west, respectively. For example, RL_90 can be further divided into RL_90_N, RL_90_S, RL_90_E, and RL_90_W, as shown in Fig. 2d. It should be noted that although the north-south direction defined here is not exactly consistent with the geographical north-south, we still define it this way for the sake of simplicity. As shown in Fig. 2c, the entire study area consists of 16 rectangular regions of interest (ROIs) with 40 m × 40 m dimensions. Additionally, two areas with non-lodging maize named NonL_N and NonL_S are set up as references. We artificially induced maize lodging according to the above experimental setup from Sep. 26–28, 2023. At this time, the maize growth stage is between R5-Dent and R6-Maturity. Fig. 2d shows an ortho-mosaic RGB image generated by the UAV-based aerial survey after maize lodging. We have to make it clear that there are certain inevitable manual errors in dimensions and lodging angles, especially in 45° lodging ROIs. Nevertheless, it is sufficient to support this exploratory study dedicated to verifying the feasibility of UAV-SAR for maize lodging monitoring.

2.2. Dataset

On August 28–29, 2023, we conducted a series of experiments based on the UAV-SAR platform (Fig. 3a). The weather during this period was mostly sunny, with temperatures ranging from 18°C to 29°C, and northerly winds of level 1–3. The UAV-SAR consists of a six-rotor UAV (KWT-X6L-15, Shenzhen, China) and two mini-SAR systems. The maximum wingspan, load capacity, flight speed, and endurance of the UAV are 2570 mm, 15 kg, 18 m/s, and approximately 30 min, respectively. Besides the two radar systems, the UAV also carries the transmitting and receiving horn antennas, the power supply system, and the independent high-precision RTK-GPS + IMU sensors. The UAV has the capability to fly fully autonomously along pre-set trajectories at a specified speed and height. The main specifications of X-band (9.6 GHz) and Ku-band (14.6 GHz) SAR systems are summarized in Table 1. The

Table 1
Specifications of X-band and Ku-band SAR systems.

Specifications	X-Band	Ku-Band
Radar mode	FMCW	FMCW
Frequency (GHz)	9.6	14.6
Band width (GHz)	1.2	1.2
Incidence angle (°)	45	45
Polarization	Quad (HH, HV, VH, VV)	Dual (HH, HV)
Scanning mode	Strip (Maximum swath is 3 km)	Strip (Maximum swath is 3 km)
Resolution (m)	Up to 0.15×0.15	Up to 0.15×0.15
Weight (kg)	≤ 3.0	≤ 3.0
Power consumption (W)	≤ 120	≤ 120

observing orientation of right-side-looking SAR is perpendicular to the UAV flight trajectory. The transmitting and receiving horn antennas are installed at a fixed angle, allowing the UAV-SAR to have a constant incidence angle of 45°. In each flight mission, X-band SAR and Ku-band SAR collect data independently and simultaneously, working in quad-polarization (HH, HV, VH, and VV) and dual-polarization (HH and VV) modes, respectively. Although the UAV-SAR imaging results can be observed in real-time on the ground control station, the raw radar and POS data are recorded in the onboard solid-state drive.

Studies have shown that the radar scattering characteristics of crops are not only affected by radar parameters but are also sensitive to the observation orientation. To study the effect of UAV-SAR's observation orientation on backscattering coefficient, we collect radar data in four orientations, namely North-South (NS), South-North (SN), West-East (WE), and East-West (EW), as shown in Fig. 3c and Fig. 3d. Due to the limitation of UAV battery endurance, two flight missions are planned according to SAR system parameters, flight height, and scope of the study area. The first flight mission (Fig. 3c) includes two working flight routes. In the first route (from waypoint #1 to waypoint #2), the UAV flights from west to east and the SAR irradiates the study area from north to south (NS). In the second route (from waypoint #3 to waypoint #4), the UAV flights from east to west and the SAR observes the study area from south to north (SN). The second flight mission (Fig. 3d) contains six working routes. The UAV-SAR irradiates the study area from west to east (WE) in three flight routes (waypoint #1 – waypoint #2, waypoint #5 – waypoint #6, and waypoint #9 – waypoint #10) and from east to west (EW) in the other three tracks (waypoint #3 – waypoint #4, waypoint #7 – waypoint #8, and waypoint #11 – waypoint #12). In each flight

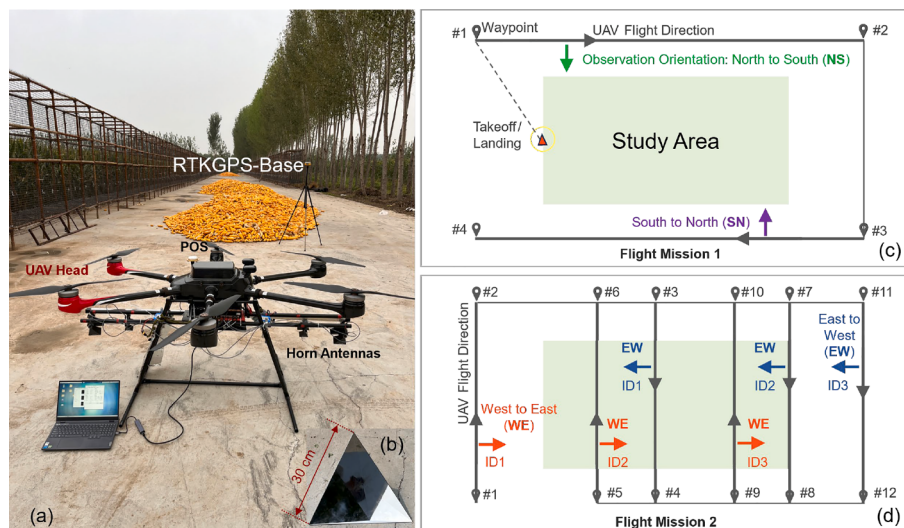


Fig. 3. UAV-SAR setup and flight mission planning. (a) X-band and Ku-band UAV-SAR systems, (b) Corner reflector, (c) The first flight mission, in which the UAV-SAR observes the study area from North to South (NS) and South to North (SN), respectively, (d) The second flight mission, in which the UAV-SAR irradiates the study area from West to East (WE) and East to West (EW), respectively.

mission, UAV-SAR takeoff from the start point and flight to the first waypoint. UAV-SAR automatically activates radar imaging at the starting point of each working route and flights towards the ending point at a constant flight height above ground of 300 m, a flight speed of 10 m/s, and a stable heading, and turns off the radar imaging after reaching the target point. After all flight missions are completed, the raw radar and POS data will be exported to the ground station for preprocessing. This procedure mainly includes radar imaging, accuracy analysis, geometric correction, orthorectification, stitching, and radiometric calibration. In this work, the backscattering coefficient (in dB) is the main metric for quantitatively analyzing the radar scattering response of different maize lodging types under different radar parameters. It is extracted from the single-looking-complex (SLC) data and calibrated by the RCS from the corner reflector (Fig. 3b). Subsequently, we use ENVI 5.6 and QGIS 3.28 to visualize, quality check, and subset the preprocessed radar data. Our evaluation results demonstrate that the spatial resolution of X-band and Ku-band radar images achieves 0.15 m/Pixel. Fig. 4 shows 24 processed polarimetric ortho-mosaic images of the study area collected by X-band and Ku-band UAV-SAR at NS, SN, WE, and EW observation orientations, respectively.

We also use the Matrice 350 RTK (SZ DJI Technology Co., Ltd., China) equipped with a gimbal ZENMUSE P1 camera to gather geocoded UAV-RGB images as ground truth to assist visual interpretation. The software running on the remote controller automatically generates the mapping mission based on preset parameters (flight height: 30 m; front overlap and side overlap: 80 %). A total of 10,696 RGB images with a

resolution of 8192×5460 are streamed into the commercial post-processing software PIX4Dfields (Ver.2.5.1) to generate the geocoded orthophoto as shown in Fig. 2d. Its file size is 31.8 GB, the dimension is $248,884 \times 63,045$ pixels, and the ground sampling distance (GSD) is approximately 3.48 mm/pixel. The 3D point cloud reconstruction was done in DJI Terra (Ver. 4.2.5), and the subsequent processing was done in ENVI LiDAR toolbox.

2.3. Methods

2.3.1. Statistical analysis of UAV-SAR data

During post-processing, we manually created 18 ROIs (Region of Interest) masking lodging and non-lodging areas in the ENVI 5.6 and generated individual ROI in <.dat> format via built-in toolboxes such as Band Stacking, ROI Subsetting, and Band Splitting. There are a total of 432 ROIs under 2 bands, 4 polarizations, and 4 observation orientations. Batch calculation of the mean, standard deviation, maximum, minimum, and quartiles of backscattering coefficients in each ROI is performed in Origin Pro (2024 SR1). This work mainly focuses on the radar back-scattering and polarization characteristics, which are widely used in spaceborne SAR remote sensing. In addition, some classic radar vegetation indices, as listed in Table 2, are also extracted by the Band Math toolbox in ENVI 5.6. Finally, we construct a total of 72 features, 24 of which are raw backscatter coefficients and 48 of which are derived radar metrics, as potential inputs for training and testing machine learning classification models. In more detail, the 24 backscatter coefficient

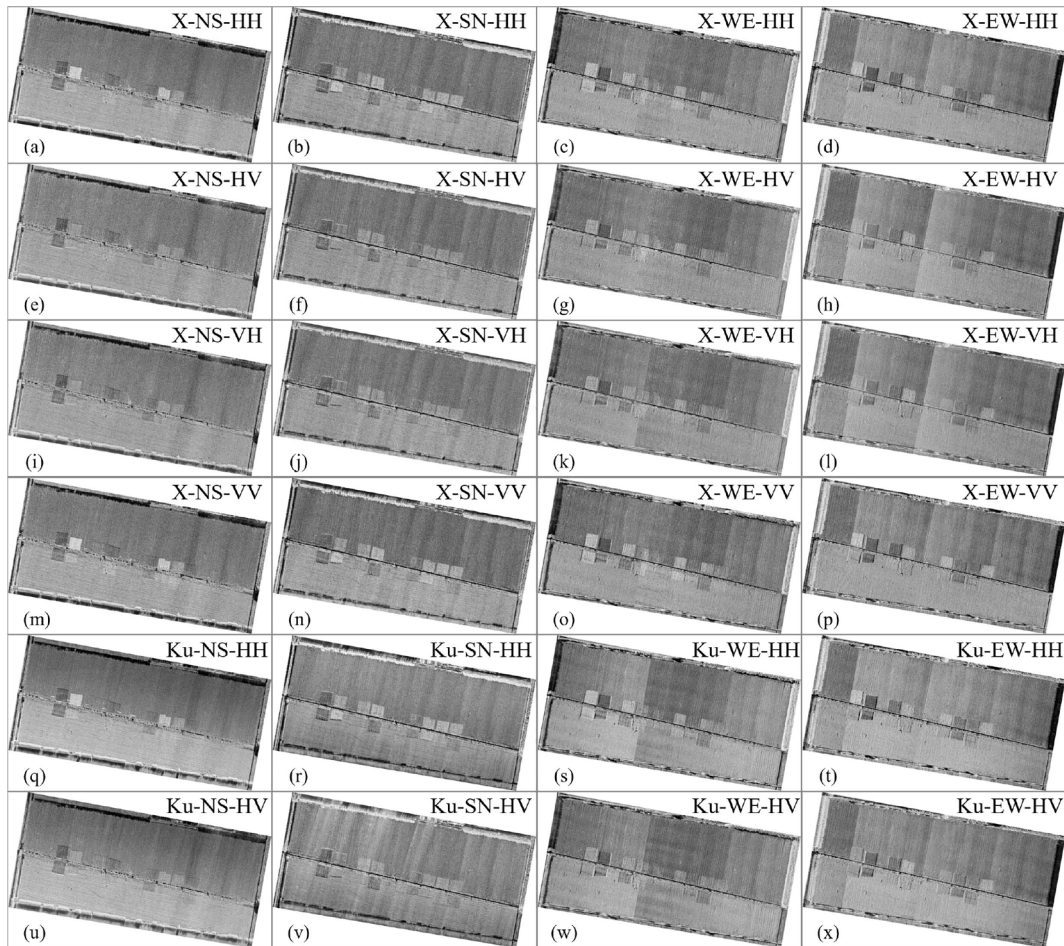


Fig. 4. Ortho-mosaic images of the study area from UAV-SAR under different radar parameters. (a)-(b) respectively shows the image of backscattering coefficients in HH, HV, VH, and VV polarizations collected by the X-band UAV-SAR at the north-to-south (NS), south-to-north (SN), west-to-east (WE) and east-to-west (EW) observation orientations, (q)-(x) respectively presents the dual polarimetric images of HH and HV gathered by Ku-band UAV-SAR from NS, SN, WE, and EW observation orientations.

Table 2
Radar vegetation indices of X-band and Ku-band UAV-SAR.

Metrics	Parameters or Formulation	Bands	Total	Ref.
Backscattering Coefficients	$\sigma_{\text{HH}}^0, \sigma_{\text{HV}}^0$	X and Ku	16	/
Backscattering Coefficients	$\sigma_{\text{VH}}^0, \sigma_{\text{VV}}^0$	X	8	/
Co-polarization Ratio (CPR)	$\sigma_{\text{VV}}^0/\sigma_{\text{HH}}^0$	X	4	Blaes et al., 2006
Cross and Co-polarization Ratio (CCPR)	$\sigma_{\text{VH}}^0/\sigma_{\text{VV}}^0$	X	4	Blaes et al., 2006
Quad-pol Radar Vegetation Index (RV _{Iquad,pol})	$8\sigma_{\text{HV}}^0/(\sigma_{\text{HH}}^0 + 2\sigma_{\text{HV}}^0 + \sigma_{\text{VV}}^0)$	X	4	Kim and van Zyl, 2009
Dual-pol Radar Vegetation Index (RV _I _{dual,pol,HH})	$4\sigma_{\text{HV}}^0/(\sigma_{\text{HH}}^0 + \sigma_{\text{HV}}^0)$	X and Ku	8	Charbonneau et al., 2005
Dual-pol Radar Vegetation Index (RV _I _{dual,pol,VV})	$4\sigma_{\text{VH}}^0/(\sigma_{\text{VV}}^0 + \sigma_{\text{VH}}^0)$	X	4	Nasirzadehdizaji et al., 2019
Canopy Structure Index (CSI)	$\sigma_{\text{VV}}^0/(\sigma_{\text{VV}}^0 + \sigma_{\text{HH}}^0)$	X	4	Pope et al., 1994
Radar Forest Degradation Index (RFDI)	$(\sigma_{\text{HH}}^0 - \sigma_{\text{HV}}^0)/(\sigma_{\text{HH}}^0 + \sigma_{\text{HV}}^0)$	X and Ku	8	Mitchard et al., 2012
Normalized Polarization (NP)	$(\sigma_{\text{VH}}^0 \cdot \sigma_{\text{VV}}^0)/(\sigma_{\text{VH}}^0 + \sigma_{\text{VV}}^0)$	X	4	Hird et al., 2017
Dual Polarization SAR Vegetation Index (DPSVI)	$\sigma_{\text{VH}}^0[(\sigma_{\text{VV(max)}}^0 \sigma_{\text{VH}}^0 - \sigma_{\text{VV}}^0 \sigma_{\text{VH(max)}}^0) + (\sigma_{\text{VV}}^0 \sigma_{\text{VH}}^0 - \sigma_{\text{VV(max)}}^0 \sigma_{\text{VH}}^0)]/(\sqrt{2} \sigma_{\text{VV}}^0 \sigma_{\text{VH}}^0)$	X	4	Periasamy, 2018
Modified DPSVI (DPSVIm)	$(\sigma_{\text{VV}}^0 + \sigma_{\text{VH}}^0 \sigma_{\text{VH}}^0)/\sqrt{2}$	X	4	dos Santos et al., 2021

features consist of 16 features (4 polarizations \times 4 observation orientations) from X-band and 8 features (2 polarizations \times 4 observation orientations) from Ku-band.

We divide each ROI in each feature into a training set and a test set at a ratio of approximately 7:3. Mean filtering with 10 filter scales ($3 \times 3, 5 \times 5, 7 \times 7, 9 \times 9, 11 \times 11, 13 \times 13, 15 \times 15, 17 \times 17, 19 \times 19$, and 21×21) without overlap is executed to suppress the inherent radar speckle noise. For instance, the GSD under 3×3 and 21×21 filter scales are approximately 0.45 m and 3.15 m, respectively. This setting is to study the impact of different filter scales on the classification accuracy of machine learning models. It should be noted that there are specific differences in the area of each lodging category, leading to a certain imbalance in the sample size of each ROI. This data imbalance may become more evident as the filter scale increases.

2.3.2. Feature selection

Feature selection is an essential preliminary work in machine learning. Its purpose is to eliminate insignificant or redundant features and construct an optimal feature subset, thereby reducing the number of features, optimizing computational complexity, improving model accuracy, and avoiding overfitting. Recursive feature elimination (RFE) is a widely used feature selection method. RFE consists of four steps: firstly, calculate the importance of each feature by an embedded machine learning model (e.g., random forest (RF)) trained based on all the features; then, the least significant feature is eliminated after sorting all features according to their importance scores; thirdly, retrain the model with the remaining features and repeat the above steps; finally, the feature combination corresponding to the highest value of the model's accuracy is selected as the ultimate result.

2.3.3. Machining learning-based classification models and evaluation metrics

Machine learning models are conventional remote sensing image intelligent interpretation methods. Five widely used machine learning-based models, namely, eXtreme Gradient Boosting XGBoost), Linear Discriminant Analysis (LDA), Random Forest (RF), K-Nearest Neighbors (KNN), and Artificial Neural Network (ANN) are used to investigate the classification performance for maize lodging type using datasets with different filter scales and feature subsets. The overall accuracy (OA) (Eq. (1)) and Kappa coefficient (Eq. (2)) across all categories are the main evaluation metrics to compare the overall classification performance of each machine learning model. In addition, four metrics, namely, accuracy (Eq. (3)), precision (Eq. (4)), recall (Eq. (5)), and F1-score (Eq. (6)), are used to evaluate their classification performance in each category.

$$\text{Overall Accuracy(OA)} = \frac{\sum_{i=1}^k TP_i}{N} \quad (1)$$

$$\text{Kappa Coefficient} = \frac{OA - p_e}{1 - p_e}, p_e = \frac{1}{N^2} \sum_{i=1}^k np_i \times nt_i \quad (2)$$

$$\text{Accuracy} = \frac{TP + TN}{TP + TN + FP + FN} \quad (3)$$

$$\text{Precision} = \frac{TP}{TP + FP} \quad (4)$$

$$\text{Recall} = \frac{TP}{TP + FN} \quad (5)$$

$$\text{F1-score} = \frac{2 \times (\text{Precision} \times \text{Recall})}{\text{Precision} + \text{Recall}} \quad (6)$$

where TP is True Positive; TN is True Negative; FP is False Positive; FN is False Negative; k is the total number of lodging and non-lodging ROIs; N is the size of the testing dataset; np_i is the number of predicted samples of the i -th category; nt_i is the number of actual samples of the i -th category.

3. Results

3.1. Distribution overview of backscattering coefficients from X-band and Ku-band UAV SAR

Fig. 5 presents the distribution of radar backscattering coefficients in 18 nonlodging and lodging ROIs. These data were collected by X-band and Ku-band UAV-SAR with four polarizations (HH, HV, VH, VV) from four orientations of (NS, SN, WE, EW). It can be seen that the overall distribution of radar backscattering coefficients within each ROI is pretty scattered, with a standard deviation of about 4 dB. Factors leading to this phenomenon include the inherent speckle noise of SAR data, the various scattering mechanisms in maize canopy, bare soil, etc. However, if extreme values and outliers are ignored, the data distribution in each ROI is still relatively concentrated according to the quartiles of the backscattering coefficient.

In this section, we mainly discuss the average backscattering coefficient (ABC) and standard deviation (SD) within each ROI, and the detailed information is also shown in Fig. 7 and Fig. 8. The first finding in Fig. 5 is that regardless of the observation orientation and lodging type, the X-band ABC of HH polarization and VV polarization are very close, with deviations less than 1.00 dB. A similar phenomenon also exists between HV and VH polarizations. Another finding is that for each ROI, the ABC of co-polarization (HH, VV) is significantly higher than that of cross-polarization (HV, VH). Taking the X_NS as an example, the ABC mean of HH polarization of 18 ROIs is 7.13 dB higher than that of HV polarization, and the ABC mean of VV polarization of 18 ROIs is 6.30 dB higher than that of VH polarization. However, the difference in ABC

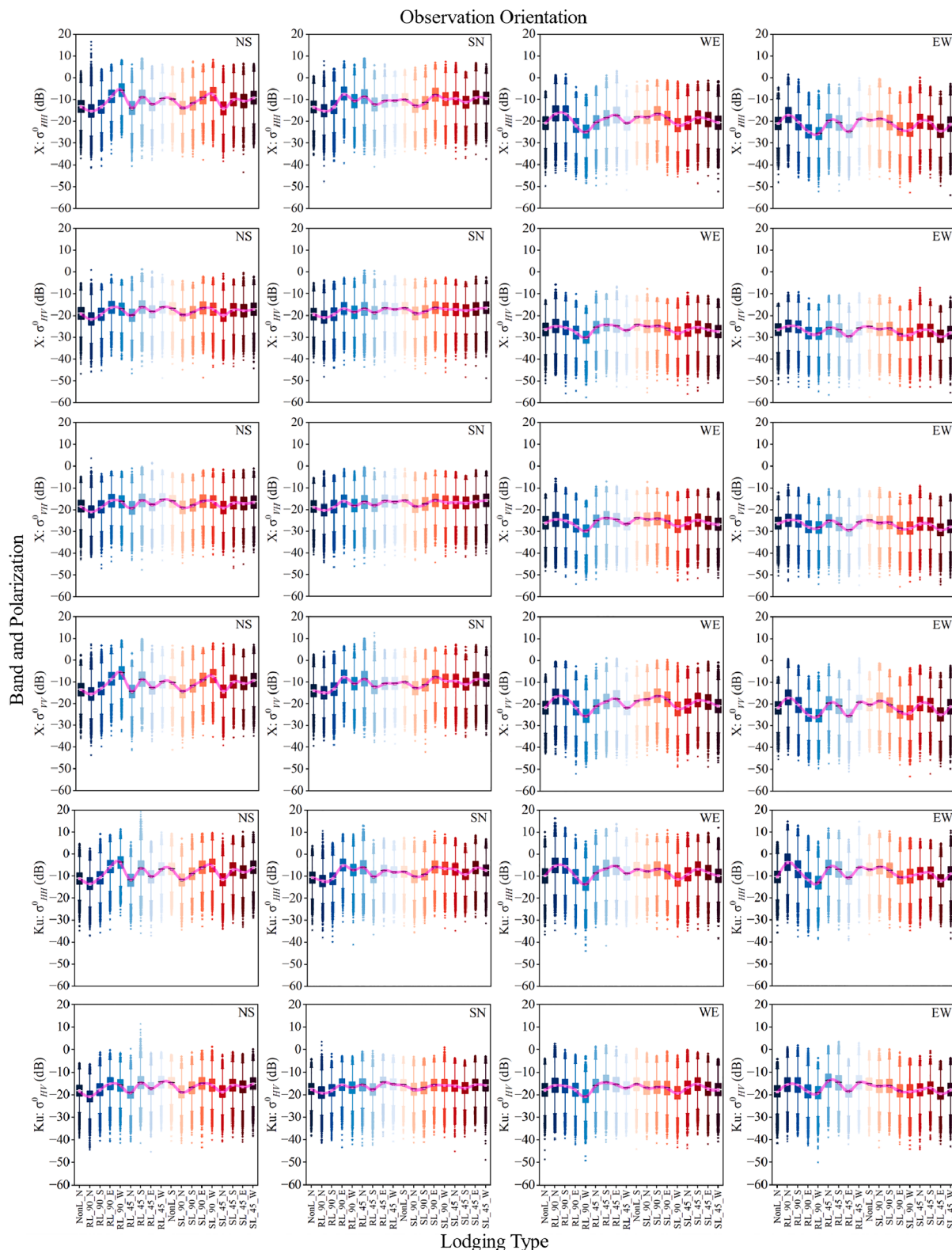


Fig. 5. Distribution of backscattering coefficients in 18 nonlodging and lodging areas with respect to bands, polarizations, and observation orientations of UAV-SAR. The purple curve fits the average backscattering coefficient of each ROI. (For interpretation of the references to color in this figure legend, the reader is referred to the web version of this article.)

mean between HH and VV is 0.19 dB, and the difference between HV and VH is 0.64 dB. Compared with X-band UAV-SAR data, the distribution of Ku-band data follows similar patterns. The third finding is that for the same lodging type, the waveband, polarization, and observation

orientation will directly affect its radar backscattering coefficient, which is also intuitively shown in Fig. 4.

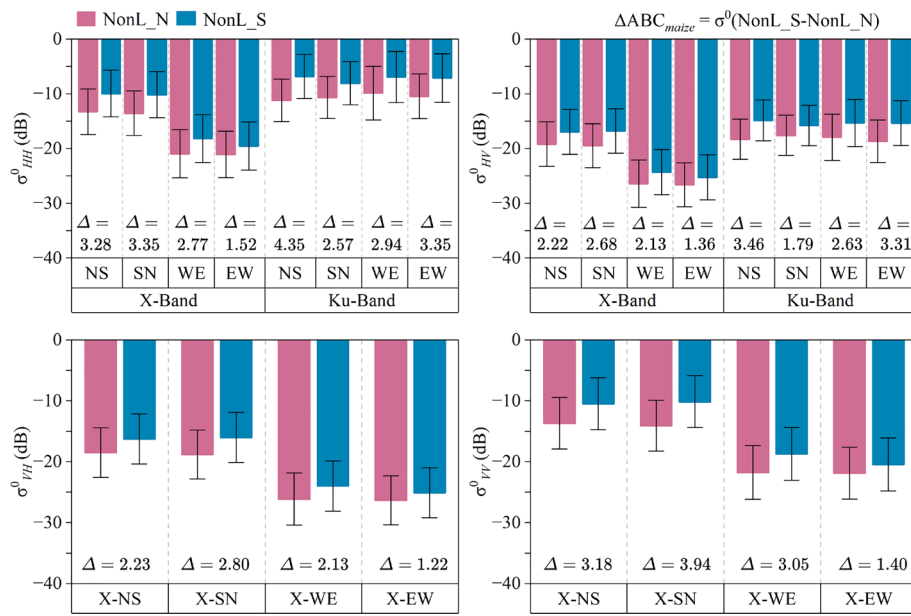


Fig. 6. Comparison of ABC with SD between two nonlodging maize breeds with respect to bands, polarizations, and observation orientations.

3.2. ABC differences between maize breeds

The ABC of UAV-SAR depends not only on radar parameters such as band, polarization, and observation orientation but also on the biophysical properties of maize. Firstly, two non-lodging areas with different breeds, named NonL_N (MY73) and NonL_S (Lenong87), are selected to analyze breed effects on UAV-SAR ABC. The ABC difference in the two regions under different experimental conditions is shown in Fig. 6. It is easy to find that regardless of the radar system parameters, the ABC of NonL_S with the non-lodging Lenong87 maize is always higher than that of NonL_N with the non-lodging MY73. Since the sowing time and management methods are almost the same in the two non-lodging ROIs, we mainly attribute these differences to maize breed variation. According to *in-situ* observations during radar data collection, the maturity of MY73 (NonL_N) is higher than that of Lenong87 (NonL_S), which means that their leaves' water and chlorophyll content are relatively low. This difference can also be observed in the RGB image shown in Fig. 2d. In general, the higher the water content of the plant, the greater the SAR backscattering coefficient, which can help explain why the ABC of NonL_S is larger than the ABC of NonL_N. This also indirectly proves that UAV-SAR has a certain potential to distinguish different crop varieties based on maturity differences. Here, we use $\Delta\text{ABC}_{\text{maize}}$ which can be calculated by subtracting the ABC of NonL_N from the ABC of NonL_S to represent the ABC difference between two nonlodging cases. The specific $\Delta\text{ABC}_{\text{maize}}$ is related to the band, polarization, and observation orientation of UAV-SAR. From the perspective of polarization, the $\Delta\text{ABC}_{\text{maize}}$ under co-polarization is greater than the $\Delta\text{ABC}_{\text{maize}}$ under cross-polarization. From the perspective of observation direction, $\Delta\text{ABC}_{\text{maize}}$ under X_SN and Ku_NS is the most significant, while $\Delta\text{ABC}_{\text{maize}}$ under X_EW and Ku_SN is the smallest. In order to fairly compare the impacts of bands, polarizations and observation orientations on ABC under different lodging types, we take NonL_S (Lenong87) as the benchmark and correct the ABC of ROIs (NonL_N, RL_90_N, RL_90_W, RL_45_N, RL_45_E, SL_90_N, SL_90_W, SL_45_N, and SL_45_E) in the MY73 planting area by adding $\Delta\sigma^0(\text{NonL}_S-\text{NonL}_N)$ under each feature respectively.

3.3. ABC differences between lodging types

Fig. 7 presents the ABC and SD of each ROI collected by X-band UAV-SAR in four polarizations (HH, HV, VH, VV) at four observation

orientations (NS, SN, WE, EW). Fig. 8 depicts the ABC and SD of each ROI collected by Ku-band UAV-SAR in two polarizations (HH, HV) at four observation orientations (NS, SN, WE, EW). Comparing Fig. 7 and Fig. 8, we can see that the changing trends of ABC with lodging types in the X-band and Ku-band are similar, although there is a numerical difference within the same ROI. This fact indicates that the same lodging type can be distinguished by the difference in radar response between the radar bands. There is no significant difference for the Ku band between the data in the east-west (WE, EW) observation orientation and the north-south (NS, SN) observation orientation. However, the X-band data are considerably lower in the east-west observation orientation than in the north-south. We attribute this phenomenon to the fact that the microwave signals of relatively low-frequency X-band are more sensitive to north-south planting ridges. Additionally, for the same lodging type, ABC usually reaches the maximum value when the observation direction is perpendicular to the lodging direction (e.g., RL_90_W and SL_45_E in X_NS; RL_90_N and SL_90_N in X_WE) and has the minimum value when the observation direction is parallel to the lodging direction (e.g., RL_90_S and SL_45_S in X_NS; RL_90_W and SL_45_W in X_WE; RL_90_E and SL_45_E in X_EW). Taking RL_45 and SL_90 as examples, their ABCs are weakly separable under the X-band NS observation orientation (X_NS) but are more distinguishable under X_SN, X_WE, and X_EW. This fact also demonstrates the necessity of using multiple observation orientations to distinguish different lodging types. As shown in Fig. 7, although the ABC of co-polarization within each ROI are very close, the difference between co-polarization and cross-polarization is significant, which is also helpful for classifying different lodging types. In summary, under different radar parameters, the ABC in different ROIs may be very close, making it impossible to distinguish the lodging types. In addition, it is difficult to effectively distinguish differences in lodging directions under the same lodging severity using the limited data from single observation. It is necessary to comprehensively use the significant features in different bands, polarizations and observation orientations to address this issue. Next, in Sections 3.4, 3.5, and 3.6, we will analyze in detail the differences in ABC under different lodging types caused by the three variables of UAV-SAR band, polarization, and observation orientation.

3.4. ABC differences between X and Ku bands

As the most important parameter of the SAR system, frequency or

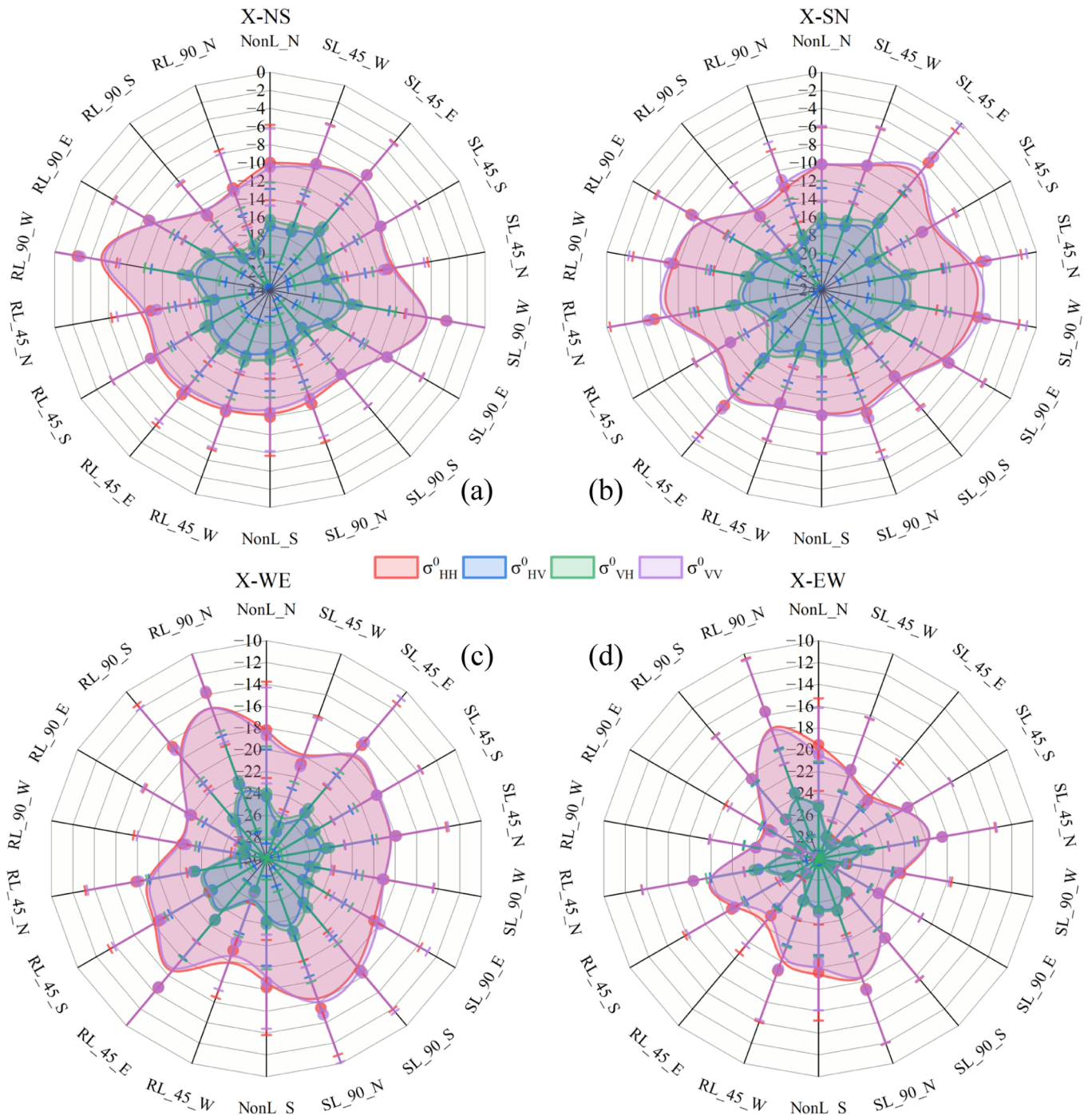


Fig. 7. ABC and SD of each ROI collected by X-band UAV-SAR in four polarizations (HH, HV, VH, VV) at four observation orientations ((a) North-South (NS), (b) South-North (SN), (c) West-East (WE), (d) East-West (EW)).

band directly affects the intensity of echoed radar signal and the penetration ability. Here, we plot Fig. 9 to compare the radar response variances with X (9.6 GHz) and Ku (14.6 GHz) in different ROIs under four observation orientations of NS, SN, WE, EW, and two polarizations of HH and HV. ΔABC_{band} represents the ABC difference between X-band and Ku-band in each ROI and is calculated by subtracting Ku from X. It can be seen that under any radar system parameters and any maize lodging scenarios, ΔABC_{band} is always less than zero, which means that the ABC of the X-band is smaller than that of the Ku-band. The differences of ΔABC_{band} mean across all ROIs in NS_HH, NS_HV (Fig. 9a-b), SN_HH, and SN_HV (Fig. 9c-d) cases are relatively small compared to that in WE_HH, WE_HV (Fig. 9e-f), EW_HH, and EW_HV (Fig. 9g-h). The

smallest ΔABC_{band} mean (-0.88 dB) appears in the SN_HV case (Fig. 9d), and the largest ΔABC_{band} mean (-13.77 dB) arises in the EW_HH case (Fig. 9g). Whether between NS and SN or between WE and EW, the differences in ΔABC_{band} mean across all ROIs are within 3 dB. However, the differences in ΔABC_{band} mean under mutually perpendicular observation orientations (such as SN and EW) can exceed 10 dB. In addition, under the four observation orientations of NS, SN, WE, and EW, the changes of ΔABC_{band} mean caused by HH and HV polarizations are 1.01 dB, 1.29 dB, 1.79 dB, and 2.61 dB, respectively.

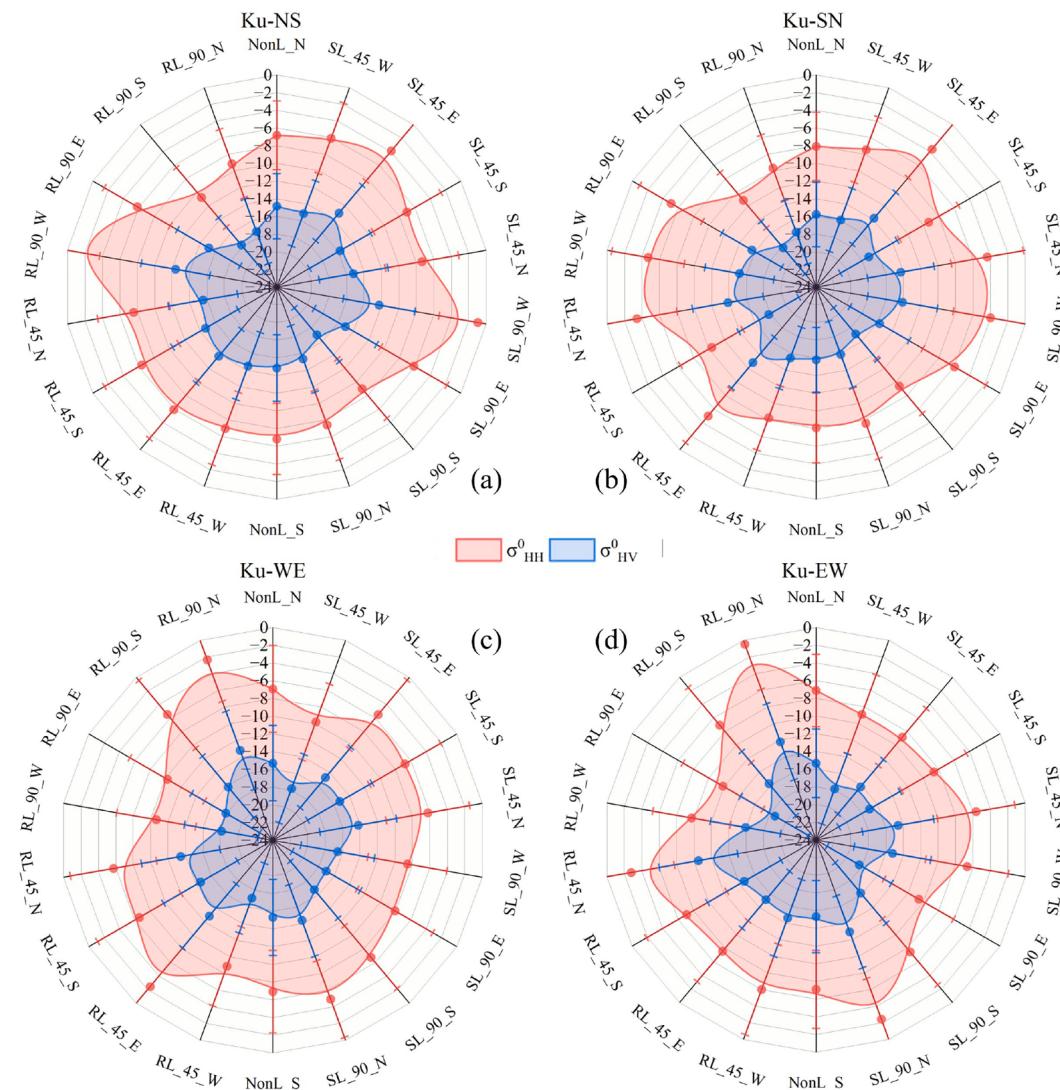


Fig. 8. ABC and SD of each ROI collected by Ku-band UAV-SAR in two polarizations (HH, HV) at four observation orientations ((a) North-South (NS), (b) South-North (SN), (c) West-East (WE), (d) East-West (EW)).

3.5. ABC differences between polarizations

Fig. 10 depicts the polarization differences of ABC ($\Delta\text{ABC}_{\text{polarization}}$) within each ROI from the X-band (Fig. 10a-d) and Ku-band (Fig. 10e) in four observation orientations. It can be found that in each ROI, there is a weak difference in the ABC for co-polarizations (HH and VV) or cross-polarizations (HV and VH), while there is a strong difference between co-polarizations and cross-polarizations, regardless of bands and observation orientations. The specific $\Delta\text{ABC}_{\text{polarization}}$ in four observation orientations is summarized in Table 3. For the X-band, the mean of absolute $\Delta\text{ABC}_{\text{polarization}}$ over 17 ROIs between HH and VV in NS, SN, WE, and EW is 0.28 dB, 0.39 dB, 0.33 dB, and 0.23 dB respectively. When it comes to HV and VH, the highest mean of absolute $\Delta\text{ABC}_{\text{polarization}}$ is only 0.67 dB in SN observation orientation. The mean of absolute $\Delta\text{ABC}_{\text{polarization}}$ between HH and HV or VV and VH are much higher than that between co-polarizations, with the lowest values of 5.75 dB and 5.41 dB, both in EW. Although the mean of absolute $\Delta\text{ABC}_{\text{polarization}}$ of the four polarimetric differences reaches the minimum value under the EW observation orientation (0.23 dB in HH-VV, 0.16 dB in HV-VH, 5.75 dB in HH-HV, and 5.41 dB in VV-VH), we can find that the polarimetric difference is generally insensitive to observation orientation. Focusing on the polarimetric difference of HH and HV, the peak occurs in X_NS_RL_90_W (12.41 dB) and Ku_NS_RL_90_W (12.83

dB), in which the observation orientation is perpendicular to the lodging direction. Comparing the mean of absolute $\Delta\text{ABC}_{\text{polarization}}$ of X-band and Ku-band, the polarimetric $\Delta\text{ABC}_{\text{polarization}}$ in HH-HV across four observation orientations ranges from 5.75 dB to 7.70 dB and from 8.36 dB to 8.79 dB respectively.

3.6. ABC differences between observation orientations

The scattering characteristics of SAR microwave signals are sensitive to the physical morphology of the observation target. Here, we will analyze the impact of UAV-SAR observation orientation on ABC under six radar system settings: X_HH, X_HV, X_VH, X_VV, Ku_HH, and Ku_HV. For each case, we calculated six orientational differences under four observation orientations, namely NS-SN, NS-WE, NS-EW, SN-WE, SN-EW, and WE-EW. The corresponding $\Delta\text{ABC}_{\text{orientation}}$ in each ROI is shown in Fig. 11. Our first finding is that the observation orientation has a significantly greater impact on X-band ABC compared to the Ku band. The mean of absolute $\Delta\text{ABC}_{\text{orientation}}$ over all ROIs in six radar system parameter settings is 7.62 dB, 6.49 dB, 6.78 dB, 7.83 dB, 2.89 dB, and 1.69 dB, respectively. Specifically, in the case of Ku_HV, the mean of absolute $\Delta\text{ABC}_{\text{orientation}}$ across all ROIs in six observation orientation differences is 1.08 dB, 1.98 dB, 2.26 dB, 1.62 dB, 1.99 dB, and 1.21 dB, as respectively shown in Table 4. The second finding is that the X-band

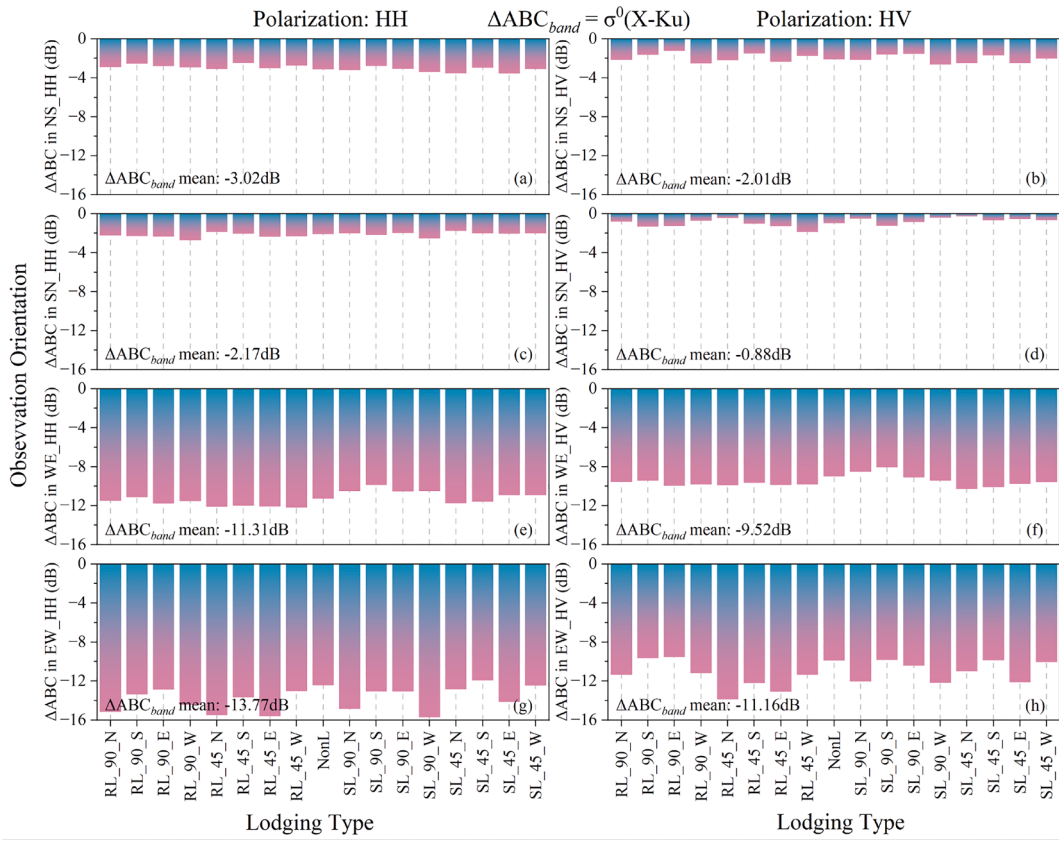


Fig. 9. ΔABC_{band} in each ROI with respect to two polarizations (HH, HV) and four observation orientations: (a) ΔABC_{band} in NS observation orientation and HH polarization, (b) ΔABC_{band} in NS observation orientation and HV polarization, (c) ΔABC_{band} in SN observation orientation and HH polarization, (d) ΔABC_{band} in SN observation orientation and HV polarization, (e) ΔABC_{band} in WE observation orientation and HH polarization, (f) ΔABC_{band} in WE observation orientation and HV polarization, (g) ΔABC_{band} in EW observation orientation and HH polarization, (h) ΔABC_{band} in EW observation orientation and HV polarization. The number in (a)-(h) is the ΔABC_{band} mean of all ROIs.

$\Delta ABC_{orientation}$ difference between orthogonal observation planes (NS-WE, NS-EW, SN-WE, SN-EW) is significantly higher than that between parallel observation planes (NS-SN, WE-EW). Amongst, the mean of absolute $\Delta ABC_{orientation}$ in SN-EW across all ROIs shows the highest value regardless of bands and polarizations, while in NS-SN holds the lowest value. This means that the features of orthogonal observation orientation of the X-band have great potential to distinguish lodging types. When it comes to the Ku band, the $\Delta ABC_{orientation}$ between orthogonal observation planes is still higher than those between parallel observation planes, although not as significant as in the X-band. The greatest mean of absolute $\Delta ABC_{orientation}$ appears in Ku_HH_NS-EW (3.81 dB). Another finding is that the observation orientation has a weak impact on the ABC of the Ku-band in the non-lodging maize area (NonL), but the impact on the ABC of the X-band cannot be ignored. This may be because the Ku has a higher frequency than the X, so the surface scattering dominates the scattering mechanisms of the maize canopy, and the Ku-band microwave signal is insensitive to the structure of maize canopy.

3.7. Feature sensitivity analysis

Coherent noise suppression is an important part of SAR signal processing. As described in Section 2.3.1, we mean-filtered the raw backscatter coefficients and the derived radar vegetation indices using 10 filter sizes ($3 \times 3, 5 \times 5, 7 \times 7, 9 \times 9, 11 \times 11, 13 \times 13, 15 \times 15, 17 \times 17, 19 \times 19$, and 21×21). As such, 10 datasets are constructed. Based on these materials, the Pearson correlation coefficients (PCCs), which can measure the strength of the linear relationship between the feature and the target variable, is calculated. The value of PCC is between -1 and 1 , with positive values representing positive correlation and negative

values indicating negative correlation. The larger the absolute value, the stronger the correlation. Specifically, we use PCCs to study the correlation between the extracted features and the lodging types. The results show that the absolute value of the PCC of each feature generally increases with the increase of the filter scale, and reaches the maximum value at 19×19 (as shown in Fig. 12), while it decreases slightly at 21×21 . It can be seen that X_NS_NP (0.240), X_NS_RVI_{dual,pol_VV} (0.240), X_NS_RVI_{quad,pol} (0.229), X_EW_DPSVI (0.223), Ku_WE_RVI_{dual,pol_HH} (0.220), X_NS_RVI_{dual,pol_HH} (0.207), X_NS_VV (0.204), Ku_NS_HH (0.195), X_WE_NP (0.167), and X_WE_RVI_{dual,pol_VV} (0.167) are the top 10 positive correlated features, while X_WE_CPR (-0.388), X_WE_CSI (-0.369), Ku_WE_HV (-0.350), X_EW_CPR (-0.322), X_EW_CSI (-0.316), Ku_EW_HV (-0.299), X_WE_HV (-0.275), Ku_WE_HH (-0.265), Ku_WE_RF DI (-0.232), and X_WE_VH (-0.209) are the top 10 negative correlated features. The average value of the absolute PCCs of the 24 backscattering coefficient features is 0.127, which is slightly higher than that of the 48 radar vegetation indices (0.116). In order to obtain the best combination of salient features, RFE feature selection is performed based on the total 72 features. Random forest (RF) is used as the embedded evaluation model of RFE and Accuracy serves as the selecting metric. A total of 50 significant features are identified by RFE and their importance ranking is shown in Fig. 13. Although the important feature sets in Fig. 13 and Fig. 14 are not exactly the same due to algorithm differences, the important features selected by RFE are highly consistent with the features with high PCC.

3.8. Classification performance evaluation of machine learning models

Five machine learning algorithms (XGBoost, LDA, RF, KNN, and

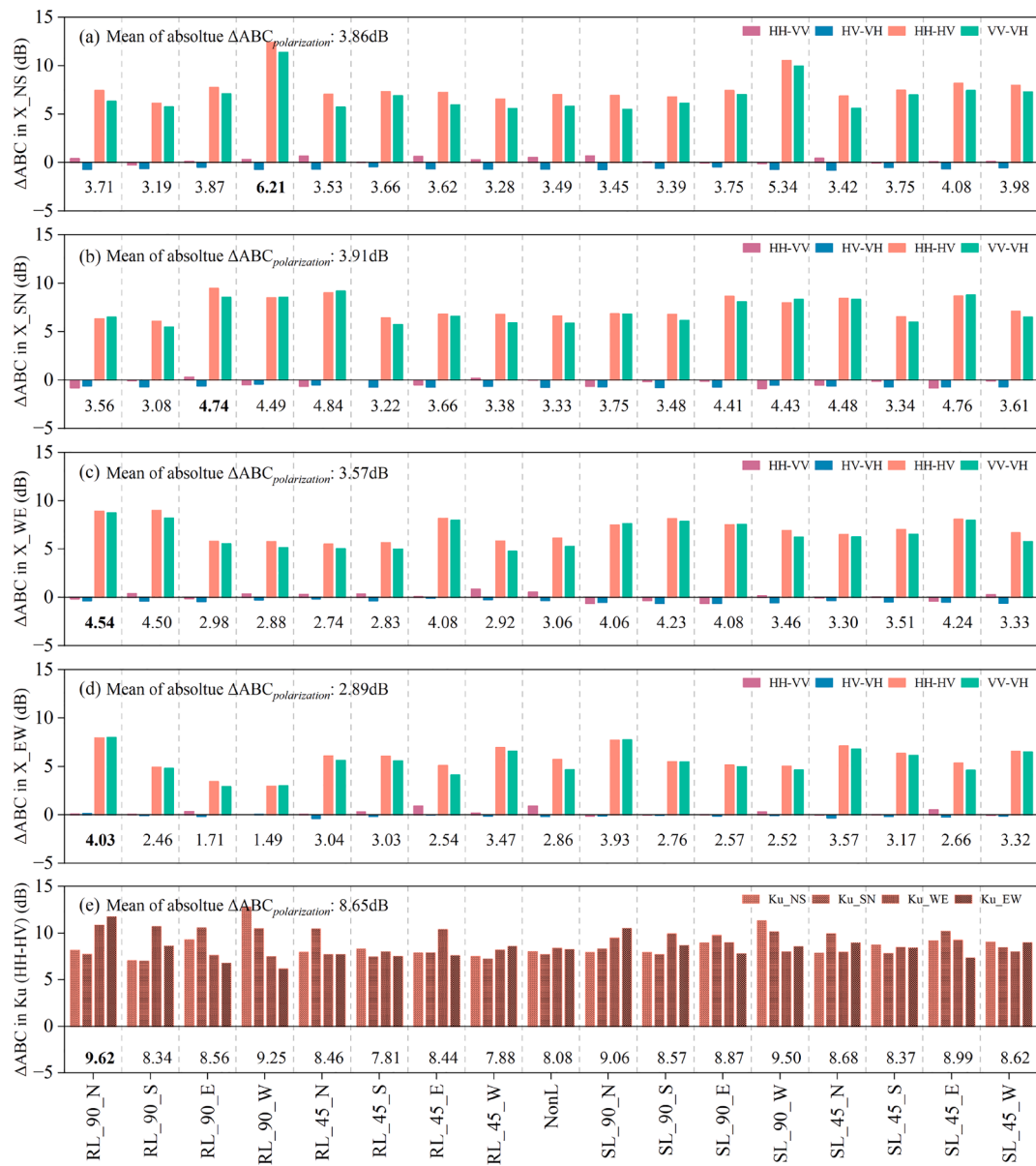


Fig. 10. $\Delta ABC_{polarization}$ in each ROI with respect to two bands and four observation orientations: (a) $\Delta ABC_{polarization}$ (HH-VV, HV-VH, HH-HV, VV-VH) from X-band UAV-SAR in North to South (NS) observation orientation, (b) $\Delta ABC_{polarization}$ from X-band in SN, (c) $\Delta ABC_{polarization}$ from X-band in WE, (d) $\Delta ABC_{polarization}$ from X-band in EW, (e) $\Delta ABC_{polarization}$ (HH-HV) from Ku-band UAV-SAR in NS, SN, WE, EW observation orientations. The number in (a)-(e) is the mean of absolute $\Delta ABC_{polarization}$ in each ROI.

Table 3

Summary of polarimetric $\Delta ABC_{polarization}$ in four observation orientations over 17 ROIs.

Band: Polarization	$\Delta ABC_{polarization}$ in NS (dB)			$\Delta ABC_{polarization}$ in SN (dB)			$\Delta ABC_{polarization}$ in WE (dB)			$\Delta ABC_{polarization}$ in EW (dB)		
	Min	Max	Abs.Mean	Min	Max	Abs.Mean	Min	Max	Abs.Mean	Min	Max	Abs.Mean
X: HH-VV	-0.26	0.66	0.28	-0.88	0.28	0.39	-0.65	0.82	0.33	-0.14	0.92	0.23
X: HV-VH	-0.81	-0.44	0.64	-0.80	-0.43	0.67	-0.63	-0.10	0.41	-0.40	0.13	0.16
X: HH-HV	6.12	12.41	7.70	6.07	9.48	7.46	5.48	8.99	7.00	2.92	7.93	5.75
X: VV-VH	5.50	11.37	6.84	5.45	9.18	7.13	4.76	8.73	6.55	2.91	8.00	5.41
Ku: HH-HV	7.04	12.83	8.71	7.00	10.55	8.75	7.48	10.86	8.79	6.18	11.75	8.36

ANN) are trained and tested based on the constructed 10 datasets with three feature combinations, namely 24 raw backscattering coefficients, 50 RFE-selected features, and 72 total features. The number of samples in the training and testing datasets within each ROI under 10 filter scales is shown in Table 5. The overall accuracy (OA) and Kappa coefficients mentioned in Section 2.3.3 are used to evaluate their classification

performance. The specific results of the OA and Kappa coefficients are shown in Table 6 and Table 7. Overall, the OA of each model increases with the increase of the filter scale and reaches the maximum at the 19×19 filter scale. It is worth noting that although the OA of KNN and ANN at the 21×21 filter scale is higher than that at 19×19 , the number of samples in each category used to train and test the machine learning

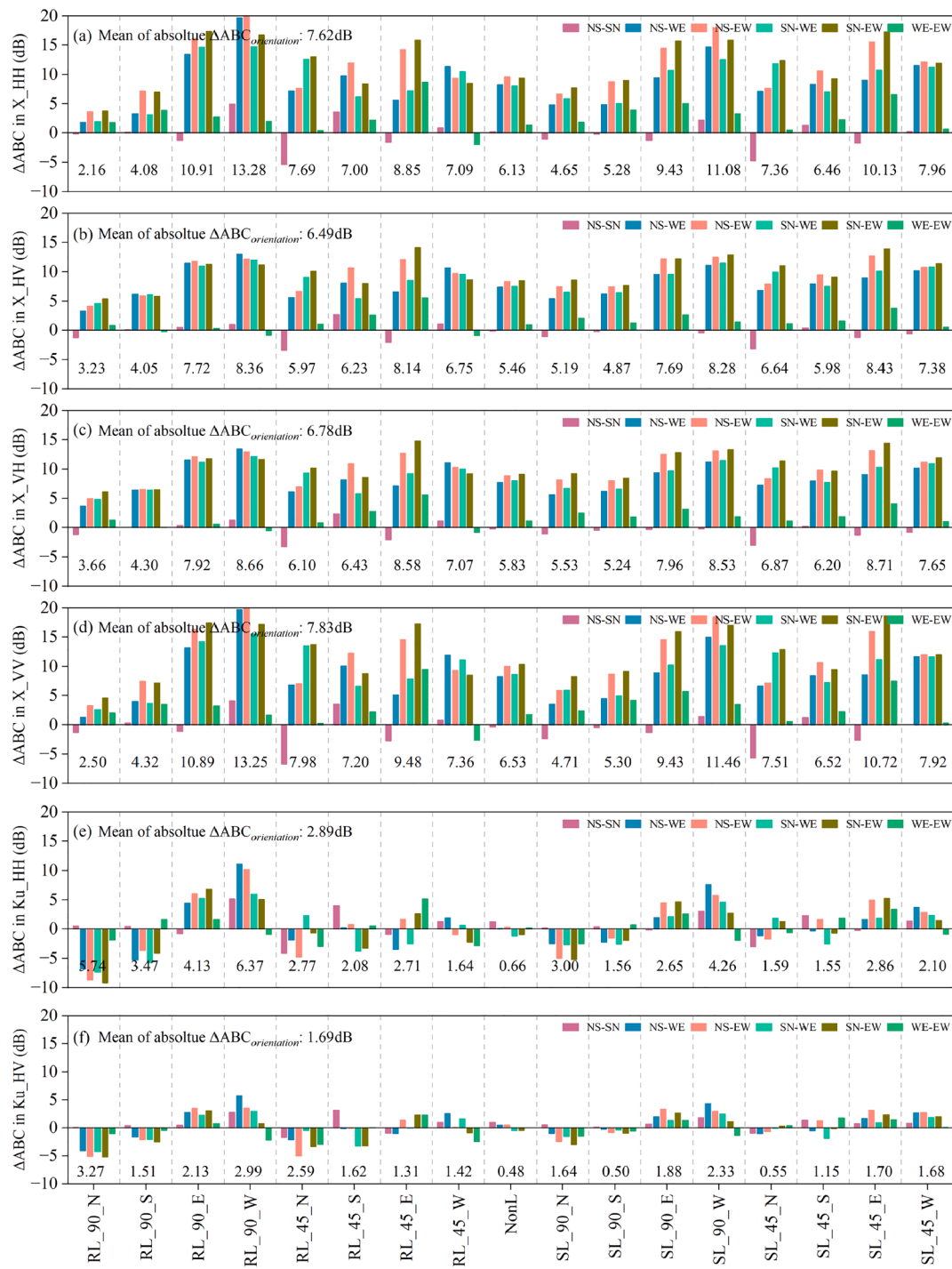


Fig. 11. $\Delta ABC_{orientation}$ in each ROI with respect to bands and polarizations: (a) $\Delta ABC_{orientation}$ in X band and HH polarization, (b) $\Delta ABC_{orientation}$ in X band and HV polarization, (c) $\Delta ABC_{orientation}$ in X band and VH polarization, (d) $\Delta ABC_{orientation}$ in X band and VV polarization, (e) $\Delta ABC_{orientation}$ in Ku band and HH polarization, (f) $\Delta ABC_{orientation}$ in Ku band and HV polarization. The number in (a)-(f) is the mean of absolute $\Delta ABC_{orientation}$ in each ROI.

models at this time is relatively small (as shown in Table 5), and overfitting may occur. In addition, as the filter scale increases, the imbalance in sample size between categories gradually becomes apparent. Therefore, we decide to use the OA and Kappa coefficient under the 19×19 filter scale as the final results. Comparing the OA of ANN under three feature combinations in Table 6, it can be found that at a smaller filter scale, using all features is beneficial to obtaining higher classification accuracy; as the filter scale increases, the best classification accuracy can also be obtained using the 50 features selected by RFE; when the filter scale is larger than 15×15 , 24 features of backscattering coefficient is

sufficient to distinguish lodging types accurately. This regular pattern basically applies to XGBoost. It can be explained by the ability of different filter scales to suppress the coherent noise of UAV-SAR. Since small filter scales have weak suppression of the noise of ABC of training samples, more features are needed to distinguish different lodging types better. However, regarding RF and KNN, the OA with 24 backscattering coefficient features generally outperforms the results under the other two feature combinations. This shows that increasing the number of features by introducing radar vegetation indices fails to improve the classification effect of RF and KNN. For LDA, the OA under the RFE

Table 4

Mean of absolute $\Delta ABC_{\text{orientation}}$ of six orientational differences in six cases over 17 ROIs.

Band_Pol.	NS-SN (dB)	NS-WE (dB)	NS-EW (dB)	SN-WE (dB)	SN-EW (dB)	WE-EW (dB)
X_HH	1.81	8.82	11.46	9.05	11.69	2.88
X_HV	1.14	8.12	9.51	8.59	9.97	1.62
X_VH	1.12	8.35	10.01	8.85	10.51	1.82
X_VV	2.12	8.64	11.44	9.43	12.22	3.10
Ku_HH	1.71	3.30	3.81	3.24	3.40	1.88
Ku_HV	1.08	1.98	2.26	1.62	1.99	1.21

feature combination can be comparable to that of ANN when the filter scale is larger than 13×13 .

ANN achieves the best classification performance among the five models, reaching 98.26 % in the OA and 0.982 in the Kappa coefficient at the 19×19 filter scale. Table 8 presents four evaluation metrics of ANN in each category with RFE features. It can be found that ANN has the relatively low F1-score in RL_90_S (0.9455), RL_90_E (0.9412), RL_45_S (0.9412), and SL_90_E (0.9375). The misclassifications are presented in the corresponding confusion matrix, as shown in Fig. 14. For RL_90_E, RL_45_S, and SL_90_E, there are 2, 3, 1 false negative (FP), and the corresponding recall is 88.89 %, 88.89 %, and 93.75 %, respectively. For RL_90_S, there are 3 false positive (FP), and the corresponding precision is 89.66 %. Additionally, we use the popular high-dimensional data visualization tool, t-SNE (t-distributed Stochastic

Neighbor Embedding), to illustrate the classification results of ANN with RFE features under the 19×19 filter scale, as shown in Fig. 15. The larger the distance between categories and the smaller the dispersion within a category, the higher the classification accuracy. It can be intuitively seen that the data discreteness in RL_90_S, RL_90_E, and RL_45_S (left red ellipse in Fig. 15) is relatively high, and the separability of part of the data in SL_90_E and SL_45_W (right red ellipse in Fig. 15) is weak. These visualization results can help explain the reasons for the misclassifications in Table 8 and Fig. 14.

4. Discussion

4.1. Using UAV-SAR to classify maize lodging types

This work is dedicated to exploring the ability of cutting-edge UAV-SAR to monitor maize lodging types. Firstly, using two micro-SAR systems with X-band and Ku-band, we collected remote sensing radar data of our study area containing lodging and non-lodging maize plants from four observation orientations. Subsequently, we analyzed the average backscattering coefficient and standard deviation under different bands, polarizations, and observation orientations within each lodging type. The results show that band, observation orientation, and polarization significantly impact the radar backscatter coefficient for the same lodging type, which is consistent with the results of previous satellite SAR crop lodging monitoring studies. Thirdly, we defined 10 filter scales to suppress the inherent coherent noise of UAV-SAR and trained five

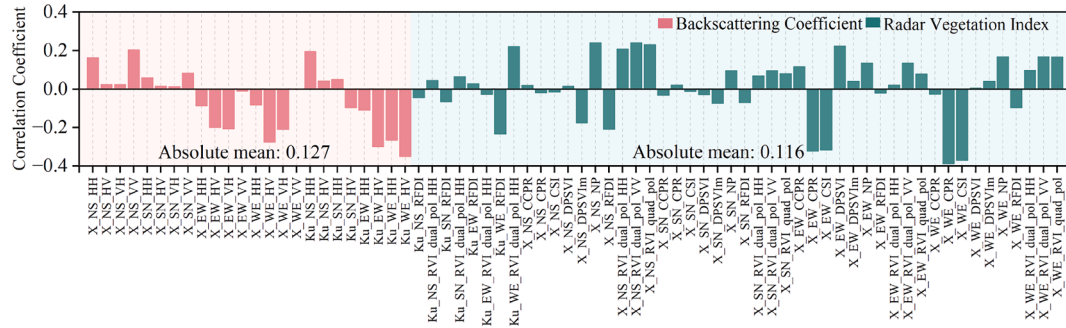


Fig. 12. Pearson correlation coefficient between features and lodging types (19×19).

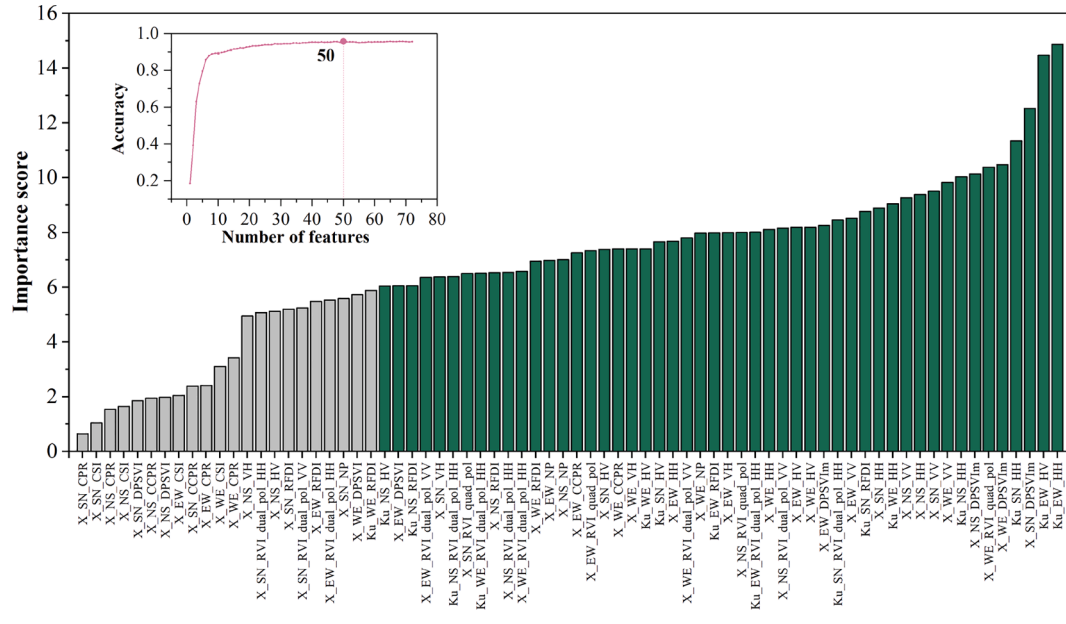


Fig. 13. Results of feature selection using RFE.

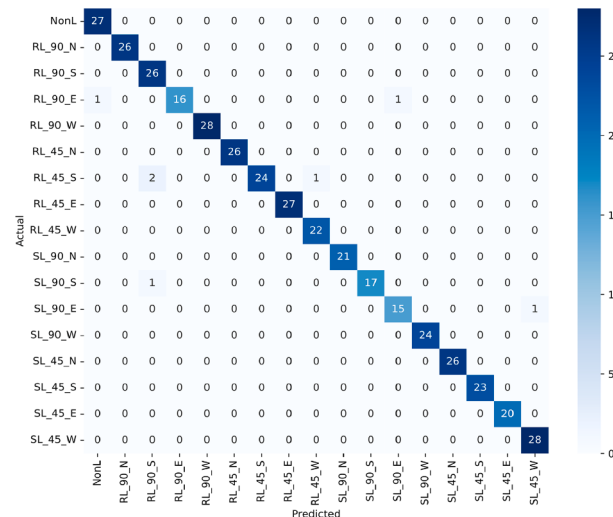


Fig. 14. Confusion matrix of classification results of ANN with RFE features under the 19×19 filter scale.

widely used machine learning-based classification algorithms using the constructed dataset and feature combinations. We found that the OA increases with the increase of the filter scale, and at 19×19 , the OA of each model exceeds 95 %.

There have been some studies on maize lodging monitoring and assessment using satellite optical, satellite SAR, and UAV optical remote sensing. Spaceborne optical and radar remote sensing are conventional means for large-scale monitoring of maize lodging. Multispectral images from Sentinel-2 and GF-1 and SAR images from Sentinel-1 and GF-3 are

the main optical and radar data sources respectively in some crop lodging monitoring studies (Guan et al., 2022a, 2022b; Qu et al., 2022, 2023). One of the most relevant works to ours is the study conducted by Guan et al. (2022a). The authors established an RF-based regional-scale lodging area estimation model based on numerous backscattering coefficients and polarization decomposition features that are extracted from the meter-level resolution Sentinel-1 and GF-3 PolSAR images. This work will be helpful in assessing the maize lodging disaster in counties or provinces scales. However, the low spatiotemporal resolution makes it difficult to accurately perceive the spatial and temporal heterogeneity of maize lodging at the field scale. In contrast, our study is dedicated to introducing UAV-SAR to make up for the limitations of satellite SAR observations at the regional scale. This is primarily attributed to two main advantages of UAV-SAR: one is the high flexibility and easy deployment of UAV-SAR, which allows it to immediately start continuous monitoring of the dynamic changes of lodging after a disaster occurs; the other is that the spatial resolution of UAV-SAR can reach 0.15 m/pixel, which is far beyond the resolution of satellite SAR, and this is conducive to obtaining fine information at regional or field scales.

UAV-based optical remote sensing is playing an increasingly important role in monitoring maize lodging. From the perspective of maize lodging parameters, the maize lodging type, area and severity are the main observed target variables, while few studies have focused on the lodging direction. From the perspective of data sources, the mainstream maize lodging monitoring methods mainly relies on UAV-based RGB, multispectral and LiDAR data (Sun et al., 2019, 2022a, 2022b; Han et al., 2022; Hu et al., 2023; Shu et al., 2023). The color and texture features extracted from UAV-RGB images are the most intuitive features for monitoring maize lodging (Wang et al., 2021). A representative work on monitoring maize lodging using UAV-RGB was done by Shu et al. (2023). They extracted and screened a variety of color and texture

Table 5
Summary of training and testing dataset with 10 filter scales.

Categories	Dataset	Filter Scales									
		3 × 3	5 × 5	7 × 7	9 × 9	11 × 11	13 × 13	15 × 15	17 × 17	19 × 19	21 × 21
NonL	Train	4653	1667	844	509	340	239	180	140	111	88
	Test	1163	416	210	127	85	59	44	34	27	22
RL_90_N	Train	4409	1582	800	483	322	228	168	131	105	84
	Test	1102	395	200	120	80	57	42	32	26	21
RL_90_S	Train	4469	1600	809	488	324	232	172	133	106	87
	Test	1117	399	202	122	81	58	42	33	26	21
RL_90_E	Train	3209	1150	583	348	232	165	122	94	74	60
	Test	802	287	145	87	58	41	30	23	18	15
RL_90_W	Train	4755	1704	863	520	344	246	184	140	113	91
	Test	1188	425	215	130	86	61	45	35	28	22
RL_45_N	Train	4451	1596	806	486	323	231	171	132	105	85
	Test	1112	399	201	121	80	57	42	32	26	21
RL_45_S	Train	4676	1677	849	512	340	240	180	140	110	91
	Test	1168	419	212	128	84	60	44	34	27	22
RL_45_E	Train	4668	1673	847	508	338	240	176	138	112	89
	Test	1166	418	211	126	84	60	44	34	27	22
RL_45_W	Train	3840	1378	698	420	278	198	146	113	90	73
	Test	959	344	174	104	69	49	36	28	22	18
SL_90_N	Train	3657	1312	663	400	264	188	141	108	86	70
	Test	914	328	165	100	65	47	35	26	21	17
SL_90_S	Train	3194	1146	580	349	232	165	122	96	75	61
	Test	798	286	144	87	57	41	30	23	18	15
SL_90_E	Train	2896	1039	524	316	209	147	111	84	68	55
	Test	723	259	131	79	52	36	27	20	16	13
SL_90_W	Train	4136	1483	752	450	299	210	160	122	99	79
	Test	1033	370	187	112	74	52	39	30	24	19
SL_45_N	Train	4412	1584	804	483	322	228	172	130	104	84
	Test	1103	396	200	120	80	56	43	32	26	21
SL_45_S	Train	4030	1443	732	440	293	207	156	120	95	78
	Test	1007	360	183	110	73	51	38	29	23	19
SL_45_E	Train	3412	1224	618	373	248	176	130	100	80	64
	Test	853	306	154	93	62	43	32	25	20	16
SL_45_W	Train	4732	1696	860	517	344	244	182	141	113	92
	Test	1182	424	214	129	85	61	45	35	28	22

Table 6

Overall accuracy (OA) of five machine learning models.

scales	XGBoost (%)			LDA (%)			RF (%)			KNN (%)			ANN (%)		
	24	RFE	72	24	RFE	72	24	RFE	72	24	RFE	72	24	RFE	72
3 × 3	62.83	66.39	70.55	62.73	63.13	62.41	60.84	62.15	62.86	60.85	59.88	59.72	65.42	72.57	78.18
5 × 5	76.52	78.67	80.61	76.91	76.36	78.22	75.09	73.98	73.70	74.13	73.31	72.35	78.00	81.82	84.34
7 × 7	84.94	84.28	85.10	84.53	84.31	84.72	83.93	81.42	81.35	82.12	80.84	80.30	84.50	87.26	88.98
9 × 9	88.60	88.34	89.18	88.23	88.71	89.18	87.86	86.54	86.12	87.34	87.12	87.07	90.13	91.87	91.72
11 × 11	91.71	92.03	91.39	91.71	89.72	92.27	90.68	89.88	89.88	91.87	91.08	91.00	92.75	93.39	93.23
13 × 13	93.93	92.24	92.24	95.61	94.83	94.94	94.49	92.46	93.36	94.15	93.36	92.80	95.73	95.73	96.06
15 × 15	94.83	93.31	93.92	95.74	96.50	96.50	94.98	94.22	94.98	94.68	95.14	94.53	96.66	97.26	96.50
17 × 17	95.64	93.86	93.27	96.83	97.03	97.03	97.43	95.25	96.04	96.04	95.64	95.45	98.22	97.03	96.04
19 × 19	97.02	96.77	95.53	97.77	98.01	98.01	98.01	97.52	97.52	97.52	97.27	96.77	98.26	98.26	98.26
21 × 21	96.32	95.09	92.94	97.55	97.85	96.01	97.85	96.93	96.63	98.16	97.24	98.47	98.16	99.08	98.16

Table 7

Kappa coefficient of five machine learning models.

scales	XGBoost			LDA			RF			KNN			ANN		
	24	RFE	72	24	RFE	72	24	RFE	72	24	RFE	72	24	RFE	72
3 × 3	0.604	0.642	0.687	0.603	0.608	0.600	0.583	0.597	0.604	0.583	0.573	0.571	0.632	0.708	0.768
5 × 5	0.750	0.773	0.794	0.754	0.749	0.768	0.735	0.723	0.720	0.725	0.716	0.706	0.766	0.807	0.833
7 × 7	0.840	0.833	0.842	0.835	0.833	0.837	0.829	0.802	0.802	0.810	0.796	0.790	0.835	0.865	0.883
9 × 9	0.879	0.876	0.885	0.875	0.880	0.885	0.871	0.857	0.852	0.865	0.863	0.862	0.895	0.914	0.912
11 × 11	0.912	0.915	0.908	0.912	0.891	0.918	0.901	0.892	0.892	0.914	0.905	0.904	0.923	0.930	0.928
13 × 13	0.935	0.917	0.917	0.953	0.945	0.946	0.941	0.920	0.929	0.938	0.929	0.923	0.955	0.955	0.958
15 × 15	0.945	0.929	0.935	0.955	0.963	0.963	0.947	0.939	0.947	0.943	0.948	0.942	0.964	0.971	0.963
17 × 17	0.954	0.935	0.928	0.966	0.968	0.968	0.973	0.949	0.958	0.958	0.954	0.952	0.981	0.968	0.958
19 × 19	0.968	0.966	0.953	0.976	0.979	0.979	0.979	0.974	0.974	0.974	0.971	0.966	0.982	0.982	0.982
21 × 21	0.961	0.948	0.925	0.974	0.977	0.958	0.977	0.967	0.964	0.980	0.971	0.984	0.980	0.990	0.980

Table 8

Evaluation metrics of ANN within each category using RFE features under the 19 × 19 filter scale.

Categories	Accuracy (%)	Precision (%)	Recall (%)	F1-score
NonL	99.75	96.43	100.00	0.9818
RL_90_N	100.00	100.00	100.00	1.0000
RL_90_S	99.26	89.66	100.00	0.9455
RL_90_E	99.50	100.00	88.89	0.9412
RL_90_W	100.00	100.00	100.00	1.0000
RL_45_N	100.00	100.00	100.00	1.0000
RL_45_S	99.26	100.00	88.89	0.9412
RL_45_E	100.00	100.00	100.00	1.0000
RL_45_W	99.75	95.65	100.00	0.9778
SL_90_N	100.00	100.00	100.00	1.0000
SL_90_S	99.75	100.00	94.44	0.9714
SL_90_E	99.50	93.75	93.75	0.9375
SL_90_W	100.00	100.00	100.00	1.0000
SL_45_N	100.00	100.00	100.00	1.0000
SL_45_S	100.00	100.00	100.00	1.0000
SL_45_E	100.00	100.00	100.00	1.0000
SL_45_W	99.75	96.55	100.00	0.9825

information from UAV-RGB orthophotos and verified the performance of various regression models and machine learning methods in estimating the severity of maize lodging (non, mild, moderate, severe). They reported that the RF achieves the highest overall accuracy of 89.47 %. Compared with UAV-RGB, UAV-multispectral is more sensitive to the dynamic changes of spectral reflectance characteristics of lodging maize. Sun et al. (2019, 2022a, 2022b) have conducted consecutive research on maize lodging severity monitoring based on the difference in spectral reflectance extracted from UAV based multispectral or hyperspectral images. A practical issue that cannot be ignored is the image quality of UAV-based RGB or multispectral is heavily dependent on the weather condition and can only be collected during daytime. The essential difference between our work and theirs is that we focus more on the changes in microwave scattering properties of maize plants in different lodging states rather than on textural and/or spectral features,

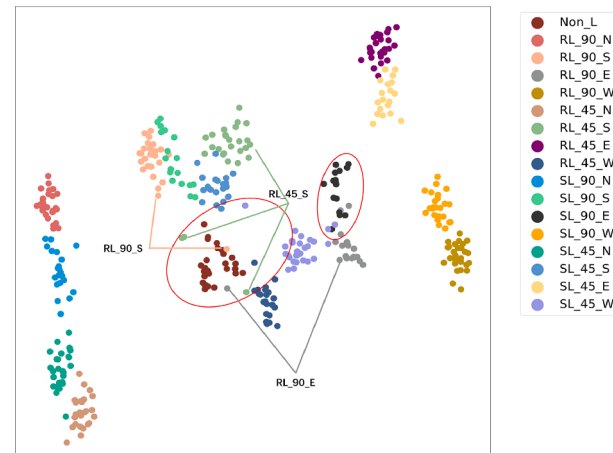


Fig. 15. t-SNE visualization of ANN with RFE features under the 19 × 19 filter scale.

which means that our proposed active UAV-SAR is capable of collecting data 24 h a day regardless of lighting conditions.

Plant height (PH) is an important feature to characterize the state of maize lodging. The corresponding canopy height model (CHM), which can be extracted by 3D point cloud reconstruction from UAV-digital-oblique/nadir orthophoto and UAV-LiDAR, is a widely used metric in maize lodging monitoring (Zhou et al., 2020b; Hu et al., 2023; Liu et al., 2024; Niu et al., 2024). For example, Niu et al. (2024) compared the plant height estimation performance by 3D reconstruction from UAV-RGB nadir and oblique imagery. Hu et al. (2023) studied the ability of UAV-RGB orthophotos, UAV-LiDAR, and backpack LiDAR to invert the canopy height and lodging angle of maize. Liu et al. (2024) comprehensively investigated the maize height estimation accuracy by oblique UAV-RGB, UAV-multispectral, and UAV-LiDAR. They concluded that LiDAR point cloud is the most accurate feature for estimating plant

height, followed by RGB oblique photography, vegetation indices, and texture features. Generally, the point clouds from UAV-LiDAR, UAV-RGB oblique, and UAV-RGB nadir imagery are more suitable for monitoring maize canopy changes caused by lodging. In this study, we also performed 2D and 3D reconstructions using nadir images acquired by the P1 camera onboard the M350-RTK UAV. The generated point cloud of the entire study area is rendered as shown in Fig. 16a and the extracted digital surface model (DSM) is shown in Fig. 16b. Fig. 16c shows the mean and standard deviation (SD) of the pH for each ROI. It can be found that there is a certain confusion in the maize PH under different lodging conditions. For example, the average PH under RL_45° root lodging and 45° stem lodging is relatively close. However, there are significant differences in the canopy structure of these two lodging states that can be captured by UAV-SAR. In addition, as shown in Fig. 16, it is difficult to distinguish different lodging directions using PH extracted from UAV nadir point clouds. Fortunately, comparing with Fig. 4, it can be seen that UAV-SAR has unique advantages in addressing this specific issue.

Although our UAV-SAR cannot directly generate point cloud data that can characterize the canopy structure, UAV-SAR can also indirectly perceive the changes in the canopy structure of lodging maize. This is mainly attributed to the scattering characteristics of microwaves in the vegetation canopy. Compared with UAV optical remote sensing, UAV-SAR also has some unique advantages. The first one is that, thanks to the wide scanning swath (e.g., approximately 500 m at 300 m flight height), UAV-SAR can collect high spatial resolution images over a large area in a single flight, which is much more efficient than UAV-RGB nadir/oblique photography or UAV-LiDAR that rely on overlapping trajectory flights. The second is that the computing resources and consuming time required for UAV-SAR post-processing are much lower than those for 3D reconstruction of UAV optical point clouds. Taking our study area as an example, the data processing of UAV-SAR only takes a few hours, while the 3D reconstruction of UAV optical images takes several days, which seriously limits the timeliness of the lodging information. The third is that the backscattering and polarization features of UAV-SAR are sensitive to the lodging direction, which is generally ignored in studies based on UAV optical remote sensing.

4.2. Limitations and prospects

To the best of our knowledge, this work is the first study fully verified

the feasibility of the cutting-edge UAV-SAR in classifying maize lodging types from UAV-SAR system construction, experimental condition design, radar data processing, data analysis, and machine learning classification. Compared with related work based on spaceborne optical, spaceborne SAR, and UAV optical remote sensing, this study demonstrated that UAV-SAR can be used as another practical technical means to efficiently and accurately classify maize lodging types. In addition, machine learning algorithms achieved high classification accuracy (more than 98 %) under the specific filter scale and feature combination.

However, we have to make it clear that this work also has certain limitations that need to be addressed in the future:

- i. This preliminary study used artificial and simplified lodging conditions. This is partly due to the lack of natural maize lodging conditions. Another consideration is to observe the radar signal response as accurately as possible by artificially controlling the spatial heterogeneity of each lodging type. This is necessary to understand the radar scattering characteristics of maize under complex natural lodging. Although artificial lodging has also appeared in some studies (Sun et al., 2022b; Hu et al., 2023), there is no doubt that the lodging parameters under natural disasters are far more complicated than those of artificial lodging. One of our top priorities is to transfer our UAV-SAR and developed methods into the natural maize lodging evaluation during different growth stages.
- ii. Due to the self-recovery ability of maize plants, lodging parameters change dynamically over time. This study focuses on the spatial heterogeneity of lodging maize but lacks exploration of temporal heterogeneity. This is our second research topic in the future real-world research.
- iii. The SAR features used in this study are limited to the backscatter coefficient and the derived radar vegetation indices. However, the polarimetric decomposition features of full-polarization and dual-polarization data are conducive to a more in-depth study of radar scattering characteristics under different maize lodging parameters. This will be another focus of our follow-up work.
- iv. Another critical parameter of the SAR system is the incidence angle. In this study, we set the incident angle of the X-band and Ku-band UAV-SAR as a constant of 45°. We will continue to conduct in-depth research on the impact of UAV-SAR incident angle on the radar response of lodging maize.

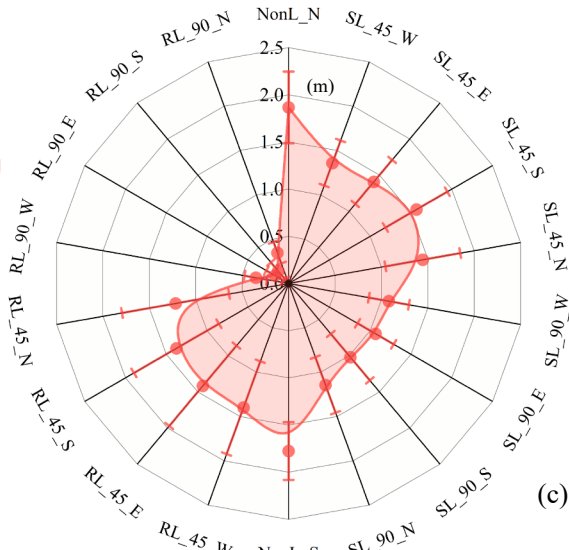
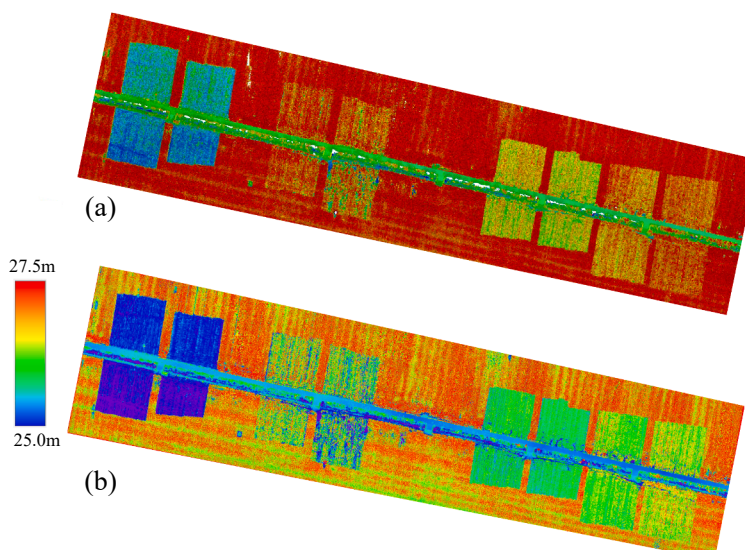


Fig. 16. Results of 3D point cloud reconstruction from nadir UAV-RGB images: (a) point clouds of study area; (b) generated digital surface model (DSM); (c) radar graph of the mean and standard deviation of pH for each ROI.

5. Conclusion

Lodging stress is one of the most common natural disasters that cause corn yield reduction. This work successfully combined UAV-SAR and machine learning for the first time to accurately classify maize lodging types. There are five main conclusions. First, the radar response of maize in different lodging types is closely related to radar parameters such as band, polarization, and observation orientations. Therefore, deep fusion of backscatter features under multiple radar parameters is the key to achieving high classification accuracy. Second, the difference in backscatter coefficient between co-polarization and cross-polarization is much more significant than that between co-polarization and copolarization. Third, radar noise suppression is an important factor limiting the classification performance. Choosing the appropriate filter scale is another key step to improve classification accuracy. Fourth, all five machine learning models can accurately distinguish different lodging types under the optimized filter scale and feature combination. Fifth, UAV SAR also has the potential to distinguish different maize breeds. This study successfully achieved high-precision maize lodging monitoring using UAV-SAR and machine learning for the first time. With the development of high-performance, highly integrated, and lightweight mini-SAR, UAV-SAR exhibits significant promise to be the fourth agricultural remote sensing technique after spaceborne optical, spaceborne SAR, and UAV-based optical remote sensing technologies.

CRediT authorship contribution statement

Dashuai Wang: Writing – original draft, Methodology, Investigation, Funding acquisition, Formal analysis, Data curation, Conceptualization. **Minghu Zhao:** Visualization, Software, Investigation, Formal analysis, Data curation. **Zhuolin Li:** Software, Investigation, Formal analysis. **Xiaohu Wu:** Writing – review & editing, Validation, Methodology. **Nan Li:** Writing – review & editing, Resources, Investigation, Funding acquisition. **Decheng Li:** Investigation, Funding acquisition, Data curation. **Sheng Xu:** Writing – review & editing, Resources, Investigation, Formal analysis. **Xiaoguang Liu:** Writing – review & editing, Validation, Supervision, Resources, Project administration, Funding acquisition.

Declaration of competing interest

The authors declare that they have no known competing financial interests or personal relationships that could have appeared to influence the work reported in this paper.

Acknowledgments

This work was supported by the National Natural Science Foundation of China (32371992), the Guangdong Basic and Applied Basic Research Foundation (2024A1515011902), the Shenzhen Science and Technology Program (JCYJ20210324102401005), the National Natural Science Foundation of China (32001424), and the Shenzhen Science and Technology Program (JCYJ20220818100408018).

Data availability

Data will be made available on request.

References

- Abushakra, F., Jeong, N., Elluru, D.N., Awasthi, A.K., Kolpuke, S., Luong, T., Reyhanigalangashi, O., Taylor, D., Gogineni, S.P., 2021. A miniaturized ultra-wideband radar for UAV remote sensing applications. *IEEE Microw. Wirel. Compon. Lett.* 32 (3), 198–201. <https://doi.org/10.1109/LMWC.2021.3129153>.
- Acevo-Herrera, R., Aguasca, A., Mallorquí, J.J., Fàbregas, X., 2009. July. High-compacted FM-CW SAR for boarding on small UAVs. In: 2009 IEEE International Geoscience and Remote Sensing Symposium. <https://doi.org/10.1109/IGARSS.2009.5418139>.
- Bekar, A., Antoniou, M., Baker, C.J., 2021. Low-cost, high-resolution, drone-borne SAR imaging. *IEEE Trans. Geosci. Remote Sensing*. 60, 1–11. <https://doi.org/10.1109/TGRS.2021.3085235>.
- Blaes, X., Defourny, P., Wegmüller, U., Della Vecchia, A., Guerrero, L., Ferrazzoli, P., 2006. C-band polarimetric indexes for maize monitoring based on a validated radiative transfer model. *IEEE Trans. Geosci. Remote Sensing*. 44 (4), 791–800. <https://doi.org/10.1109/TGRS.2005.860969>.
- Charbonneau, F., Trudel, M., Fernandes, R., 2005. Use of dual polarization and multi-incidence SAR for soil permeability mapping. In: Proceedings of the 2005 Advanced Synthetic Aperture Radar (ASAR) Workshop, pp. 15–17.
- Chauhan, S., Darvishzadeh, R., Boschetti, M., Pepe, M., Nelson, A., 2019. Remote sensing-based crop lodging assessment: Current status and perspectives. *ISPRS-J. Photogramm. Remote Sens.* 151, 124–140. <https://doi.org/10.1016/j.isprsjprs.2019.03.005>.
- Chauhan, S., Darvishzadeh, R., Lu, Y., Boschetti, M., Nelson, A., 2020. Understanding wheat lodging using multi-temporal Sentinel-1 and Sentinel-2 data. *Remote Sens. Environ.* 243, 111804. <https://doi.org/10.1016/j.rse.2020.111804>.
- dos Santos, E.P., Da Silva, D.D., do Amaral, C.H., 2021. Vegetation cover monitoring in tropical regions using SAR-C dual-polarization index: seasonal and spatial influences. *Int. J. Remote Sens.* 42 (19), 7581–7609. <https://doi.org/10.1080/01431161.2021.1959955>.
- Guan, H., Huang, J., Li, L., Li, X., Ma, Y., Niu, Q., Huang, H., 2022a. A novel approach to estimate maize lodging area with PolSAR data. *IEEE Trans. Geosci. Remote Sensing*. 60, 1–17. <https://doi.org/10.1109/TGRS.2022.3216341>.
- Guan, H., Huang, J., Li, X., Zeng, Y., Su, W., Ma, Y., Dong, J., Niu, Q., Wang, W., 2022b. An improved approach to estimating crop lodging percentage with Sentinel-2 imagery using machine learning. *Int. J. Appl. Earth Obs. Geoinf.* 113, 102992. <https://doi.org/10.1016/j.jag.2022.102992>.
- Han, L., Yang, G., Yang, X., Song, X., Xu, B., Li, Z., Wu, J., Yang, H., Wu, J., 2022. An explainable XGBoost model improved by SMOTE-ENN technique for maize lodging detection based on multi-source unmanned aerial vehicle images. *Comput. Electron. Agric.* 194, 106804. <https://doi.org/10.1016/j.compag.2022.106804>.
- Hashemi, M.G., Jalilvand, E., Alemohammad, H., Tan, P.N., Das, N.N., 2024. Review of synthetic aperture radar with deep learning in agricultural applications. *ISPRS-J. Photogramm. Remote Sens.* 218, 20–49. <https://doi.org/10.1016/j.isprsjprs.2024.08.018>.
- Hird, J.N., DeLancey, E.R., McDermid, G.J., Kariyeva, J., 2017. Google Earth Engine, open-access satellite data, and machine learning in support of large-area probabilistic wetland mapping. *Remote Sens.* 9 (12), 1315. <https://doi.org/10.3390/rs9121315>.
- Hu, X., Gu, X., Sun, Q., Yang, Y., Qu, X., Yang, X., Guo, R., 2023. Comparison of the performance of Multi-source Three-dimensional structural data in the application of monitoring maize lodging. *Comput. Electron. Agric.* 208, 107782. <https://doi.org/10.1016/j.compag.2023.107782>.
- Hügler, P., Roos, F., Schartel, M., Geiger, M., Waldschmidt, C., 2018. Radar taking off: New capabilities for UAVs. *IEEE Microw. Mag.* 19 (7), 43–53. <https://doi.org/10.1109/MMM.2018.2862558>.
- Kim, Y., Van Zyl, J.J., 2009. A time-series approach to estimate soil moisture using polarimetric radar data. *IEEE Trans. Geosci. Remote Sensing*. 47 (8), 2519–2527. <https://doi.org/10.1109/TGRS.2009.2014944>.
- Liu, T., Zhu, S., Yang, T., Zhang, W., Xu, Y., Zhou, K., Wu, W., Zhao, Y., Yao, Z., Yang, G., Wang, Y., Sun, C., Sun, J., 2024. Maize height estimation using combined unmanned aerial vehicle oblique photography and LiDAR canopy dynamic characteristics. *Comput. Electron. Agric.* 218, 108685. <https://doi.org/10.1016/j.compag.2024.108685>.
- Maes, W.H., Steppe, K., 2019. Perspectives for remote sensing with unmanned aerial vehicles in precision agriculture. *Trends Plant Sci.* 24 (2), 152–164. <https://doi.org/10.1016/j.tpls.2018.11.007>.
- Mitchard, E.T.A., Saatchi, S.S., White, L.J.T., Abernethy, K.A., Jeffery, K.J., Lewis, S.L., Collins, M., Lefsky, M.A., Leal, M.E., Woodhouse, I.H., Meir, P., 2012. Mapping tropical forest biomass with radar and spaceborne LiDAR in Lopé National Park, Gabon: overcoming problems of high biomass and persistent cloud. *Biogeosciences* 9 (1), 179–191. <https://doi.org/10.5194/bg-9-179-2012>.
- Moreira, A., Prats-Iriola, P., Younis, M., Krieger, G., Hajnsek, I., Papathanassiou, K.P., 2013. A tutorial on synthetic aperture radar. *IEEE Geosci. Remote Sens. Mag.* 1 (1), 6–43. <https://doi.org/10.1109/MGRS.2013.2248301>.
- Nasrizadehdizaji, R., Balık Sanlı, F., Abdikan, S., Cakir, Z., Sekertekin, A., Ustuner, M., 2019. Sensitivity analysis of multi-temporal Sentinel-1 SAR parameters to crop height and canopy coverage. *Appl. Sci.* 9 (4), 655. <https://doi.org/10.3390/app9040655>.
- Niu, Y., Han, W., Zhang, H., Zhang, L., Chen, H., 2024. Estimating maize plant height using a crop surface model constructed from UAV RGB images. *Biosyst. Eng.* 241, 56–67. <https://doi.org/10.1016/j.biosystemseng.2024.04.003>.
- Periasamy, S., 2018. Significance of dual polarimetric synthetic aperture radar in biomass retrieval: An attempt on Sentinel-1. *Remote Sens. Environ.* 217, 537–549. <https://doi.org/10.1016/j.rse.2018.09.003>.
- Pinthus, M.J., 1974. Lodging in wheat, barley, and oats: the phenomenon, its causes, and preventive measures. *Adv. Agron.* 25, 209–263. [https://doi.org/10.1016/S0065-2113\(08\)60782-8](https://doi.org/10.1016/S0065-2113(08)60782-8).
- Pope, K.O., Rey-Benayas, J.M., Paris, J.F., 1994. Radar remote sensing of forest and wetland ecosystems in the Central American tropics. *Remote Sens. Environ.* 48 (2), 205–219. [https://doi.org/10.1016/0034-4257\(94\)90142-2](https://doi.org/10.1016/0034-4257(94)90142-2).
- Qu, X., Shi, D., Gu, X., Sun, Q., Hu, X., Yang, X., Pan, Y., 2022. Monitoring lodging extents of maize crop using multitemporal GF-1 images. *IEEE J. Sel. Top. Appl. Earth*

- Observ. Remote Sens. 15, 3800–3814. <https://doi.org/10.1109/JSTARS.2022.3170345>.
- Qu, X., Zhou, J., Gu, X., Wang, Y., Sun, Q., Pan, Y., 2023. Monitoring maize lodging severity based on multi-temporal Sentinel-1 images using Time-weighted Dynamic time Warping. Comput. Electron. Agric. 215, 108365. <https://doi.org/10.1016/j.compag.2023.108365>.
- Remy, M.A., de Macedo, K.A., Moreira, J.R., 2012. July. The first UAV-based P-and X-band interferometric SAR system. In: 2012 IEEE International Geoscience and Remote Sensing Symposium. <https://doi.org/10.1109/IGARSS.2012.6352478>.
- Romero-Puig, N., Lopez-Sanchez, J.M., 2021. A review of crop height retrieval using InSAR strategies: Techniques and challenges. IEEE J. Sel. Top. Appl. Earth Observ. Remote Sens. 14, 7911–7930. <https://doi.org/10.1109/JSTARS.2021.3100874>.
- Shu, M., Bai, K., Meng, L., Yang, X., Li, B., Ma, Y., 2023. Assessing maize lodging severity using multitemporal UAV-based digital images. Eur. J. Agron. 144, 126754. <https://doi.org/10.1016/j.eja.2023.126754>.
- Sun, Q., Chen, L., Xu, X., Gu, X., Hu, X., Yang, F., Pan, Y., 2022a. A new comprehensive index for monitoring maize lodging severity using UAV-based multi-spectral imagery. Comput. Electron. Agric. 202, 107362. <https://doi.org/10.1016/j.compag.2022.107362>.
- Sun, Q., Sun, L., Shu, M., Gu, X., Yang, G., Zhou, L., 2019. Monitoring maize lodging grades via unmanned aerial vehicle multispectral image. Plant Phenomics, 2019. 10.34133/2019/5704154.
- Sun, Q., Gu, X., Chen, L., Xu, X., Wei, Z., Pan, Y., Gao, Y., 2022b. Monitoring maize canopy chlorophyll density under lodging stress based on UAV hyperspectral imagery. Comput. Electron. Agric. 193, 106671. <https://doi.org/10.1016/j.compag.2021.106671>.
- Wang, Z., Nie, C., Wang, H., Ao, Y., Jin, X., Yu, X., Bai, Y., Liu, Y., Shao, M., Cheng, M., Liu, S., Wang, S., Tuohuti, N., 2021. Detection and analysis of degree of maize lodging using UAV-RGB image multi-feature factors and various classification methods. ISPRS Int. J. Geo-Inf. 10 (5), 309. <https://doi.org/10.3390/ijgi10050309>.
- Wang, Z., Ding, Z., Sun, T., Zhao, J., Wang, Y., Zeng, T., 2023. UAV-Based P-Band SAR tomography with long baseline: a multi-master approach. IEEE Trans. Geosci. Remote Sensing. 61, 5207221. <https://doi.org/10.1109/TGRS.2023.3272039>.
- Xing, M., Jiang, X., Wu, R., Zhou, F., Bao, Z., 2009. Motion compensation for UAV SAR based on raw radar data. IEEE Trans. Geosci. Remote Sensing. 47 (8), 2870–2883. <https://doi.org/10.1109/TGRS.2009.2015657>.
- Yang, H., Chen, E., Li, Z., Zhao, C., Yang, G., Pignatti, S., Casa, R., Zhao, L., 2015. Wheat lodging monitoring using polarimetric index from RADARSAT-2 data. Int. J. Appl. Earth Obs. Geoinf. 34, 157–166. <https://doi.org/10.1016/j.jag.2014.08.010>.
- Zhou, L., Cheng, S., Sun, Q., Gu, X., Yang, G., Shu, M., Feng, H., 2020a. Remote sensing of regional-scale maize lodging using multitemporal GF-1 images. J. Appl. Remote Sens. 14 (01), 1. <https://doi.org/10.1117/1.JRS.14.014514>.
- Zhou, L., Gu, X., Cheng, S., Yang, G., Shu, M., Sun, Q., 2020b. Analysis of plant height changes of lodged maize using UAV-LiDAR data. Agriculture 10 (5), 146. <https://doi.org/10.3390/agriculture10050146>.